Combination of machine learning and protein-protein interaction network established one ATM-DPP4-TXN ferroptotic diagnostic model with experimental validation

MENGZE WU[1,2*], ZHAO ZOU[1,2*], YUCE PENG[1,2] and SUXIN LUO[1,2]

[1]Division of Cardiology, The First Affiliated Hospital of Chongqing Medical University, Yuzhong, Chongqing 400016, P.R. China; [2]Cardiovascular Disease Laboratory, Chongqing Medical University, Yuzhong, Chongqing 400016, P.R. China

Received February 18, 2025; Accepted June 11, 2025

DOI: 10.3892/mmr.2025.13604

Abstract. Ferroptosis and lethal sepsis are interlinked, although this association remains largely unknown to clinical panels. Sepsis is characterized by dysfunction of the inflammatory microenvironment. Most septic biomarkers lack independent validation, and a comprehensive diagnosis comprising biomarker assessment combined with clinical evaluation may improve sepsis management. Targeting ferroptosis regulators may offer new hope for uncovering the inflammatory machinery and for developing novel diagnostic methods for sepsis, and bioinformatics analyses are a valuable tool to investigate this further. In the present study, septic datasets were obtained from the Gene Expression Omnibus database. Differentially expressed genes (DEGs) were subsequently introduced in enrichment analyses and intersected with ferroptotic genes for acquiring ferroptosis-related DEGs (FRDEGs). A protein-protein interaction network (PPIN) was then constructed to retain hub-FRDEGs, and this was imported into three machine learning algorithms. A nomogram based on the logistic regression model was subsequently built and validated *in silico*. CIBERSORT and single-sample gene set enrichment analysis were used to carry out an analysis of the immune microenvironment, and inflammatory associations with the hub-FRDEGs were examined. A cellular model was subsequently applied to substantiate the results of the bioinformatic analyses. A total of 94 FRDEGs were obtained from the overlap of 4,410 DEGs and 506 ferroptotic genes. One PPIN of FRDEGs was constructed to identify 38 hub-FRDEGs, and the three machine learning algorithms were subsequently analyzed, which resulted in the identification of three hub-FRDEGs, namely ataxia telangiectasia mutated, dipeptidyl peptidase 4 and thioredoxin. One diagnostic nomogram was advanced and scrutinized for its diagnostic accuracy. The functions and pathways of the DEGs were revealed to be mainly concentrated on the immune response and cellular transportation. A notably wide discrepancy was demonstrated to exist between the hub-FRDEGs and the immunocytes. In conclusion, three potential hub-FRDEGs connected with sepsis were identified in the present study. Their diagnostic accuracy and immune association demonstrated that ferroptosis is implicated in the inflammatory dysfunction of sepsis, and based on these findings, novel strategies for pharmacological interference and improving diagnostic utility may be developed to facilitate improved management of sepsis.

Correspondence to: Dr Yuce Peng, Cardiovascular Disease Laboratory, Chongqing Medical University, 1 Yixueyuan Road, Yuzhong, Chongqing 400016, P.R. China
E-mail: china.pyc@live.com

Dr Suxin Luo, Division of Cardiology, The First Affiliated Hospital of Chongqing Medical University, 1 Youyi Road, Yuzhong, Chongqing 400016, P.R. China
luosuxin@hospital.cqmu.edu.cn

*Contributed equally

Abbreviations: ACSL4, acyl CoA synthetase long chain family member 4; AUC, area under curve; ATM, ataxia telangiectasia mutated; BP, biological process; CC, cellular component; CDF, cumulative distribution function; DEGs, differentially expressed genes; DPP4, dipeptidyl peptidase 4; FRDEGs, ferroptosis related DEGs; FRGs, ferroptosis related genes; GEO, Gene Expression Omnibus; GO, Gene Ontology; GSVA, gene set variation analysis; GPX4, glutathione peroxidase 4; oxidized glutathione; GSSG; KEGG, Kyoto Encyclopaedia of Genes and Genomics; LASSO, least absolute shrinkage and selection operator; LPS, lipopolysaccharide; MF, molecular function; MDA, malondialdehyde; si, small interfering; NC, negative control; NCOA4, nuclear receptor coactivator 4; NK, natural killer; OD, optical density; PMA, phorbol myristate acetate; PCA, principal component analysis; PPIN, protein protein interaction network; ROC, receiver operating characteristic; Tregs, regulatory T Cells; RMA, robust multiarray averaging; ssGSEA, single sample gene set enrichment analysis; STRING, Search Tool for the Retrieval of Interacting Genes/Proteins; SGLT2, sodium glucose cotransporter 2; SVM-RFE, support vector machine-recursive feature elimination; TXN, thioredoxin

Key words: sepsis, ferroptosis, immune microenvironment, ataxia telangiectasia mutated, DPP4, thioredoxin

Introduction

The incidence of sepsis globally has been estimated at 48.9 million, and sepsis accounts for 19.7% of worldwide cases

of mortality (1). Resulting from infections, sepsis management is important for patients given the high mortality rate in hospitals (>10%) (2), and therefore the rapid diagnosis of sepsis is important. Biomarkers have been revealed to be invaluable in terms of differentiating and predicting the prognoses for suspected septic cases (3). However, the majority of septic biomarkers need to be validated and evaluated independently of their clinical utility (4). Therefore, the deficiencies that currently exist in the knowledge of diagnosing sepsis act as a stimulant for the development and validation of novel septic diagnostic utilities.

Ferroptosis is a type of regulated cell death that is characterized by iron-dependent metabolic imbalance and phospholipid peroxidation (5). The enzyme glutathione (GSH) peroxidase 4 (GPX4) serves a role in monitoring the level of lipidic oxidative stress, and an increase in GPX4 leads to a decrease in the level of oxidative stress resulting from phospholipid peroxidation; therefore, either reducing the level of this enzyme, or impairing its activity, may commit the cells to ferroptosis (5). Inflammation and ferroptosis are interlinked: Inflammation may trigger ferroptosis (6), whereas a previous study demonstrated that the latter may amplify inflammation (7). Regarding sepsis, ferroptosis and immune microenvironment dysfunction are implicated in this process, and both exercise mediatory roles in its progression. Ferroptosis has been revealed to exacerbate sepsis induced encephalopathy, cardiomyopathy, acute lung injury and acute kidney injury (8). Methyltransferase-like 3 contributes to septic acute lung injury via neutrophil extracellular traps-mediated m6A modification, and subsequently, alveolar epithelial cellular ferroptosis (9), whereas the nuclear factor, interleukin 3 regulated-acyl-CoA synthetase long-chain family member 4 (ACSL4) signaling axis was revealed to regulate ferroptosis and inflammation in septic acute kidney injury (10). However, additional studies are required to properly delineate the roles of ferroptosis and immune infiltration in septic pathogenesis and development.

The present study has concentrated on screening and validating novel septic biomarkers from the perspective of their involvement in ferroptosis and their inflammatory roles in sepsis. The aim was to analyze septic transcriptomic data via next-generation sequencing, and candidate biomarkers were selected using a protein-protein interaction network (PPIN) and machine learning algorithms. The diagnostic accuracy of the candidate biomarkers was then investigated separately and holistically, and their correlation with the immune microenvironment was analyzed using immune infiltration scoring. Subsequently, *in vitro* experiments were designed to experimentally validate the bioinformatics results, which identified three potential hub ferroptosis-related differentially expressed genes (FRDEGs) that were shown to be associated with sepsis. Taken together, the findings of the present study have provided a promising and practical contribution to the diagnosis and management of sepsis.

Materials and methods

Data collection. Sepsis-associated gene expression datasets were obtained from the Gene Expression Omnibus (GEO) database (ncbi.nlm.nih.gov/geo/) searching the keywords 'sepsis' and 'Homo sapiens'. The transcriptomic datasets that were selected were required to conform to the following criteria (11): i) Samples had been collected from whole blood; ii) samples contained healthy control and septic patients (in a state of either sepsis or septic shock); and iii) the sample size was >50. Ultimately, four datasets (dataset nos. GSE185263, GSE57065, GSE131761 and GSE95233) were downloaded from the GEO database. Of these datasets, GSE185263 was the only one generated by a high-throughput sequencing platform, the other datasets were generated by a microarray platform.

The batch effect from experimental restrictions in data batches often impedes subsequent analysis with statistical heterogeneity (12), and the dataset bias from the significant difference in the principle and measurement of microarray data (the continuous measurement on the signal sensitivity of probes) (13) and high-throughput data (integer counts on the copy number of transcripts) (14) causes the incomparability of transcriptomic profiling (15). The design of two previous septic studies were consulted (11,16) to avoid the batch effect and dataset bias simultaneously. The authors had selected one high-throughput dataset and multiple microarray datasets and separately used each dataset by using the high-throughput dataset as a training cohort and microarray datasets as independent external validations. Following the aforementioned precedents, GSE185263 (high-throughput dataset) was assigned as the training cohort and the three other microarray datasets (GSE57065, GSE131761, and GSE95233) were assigned as the independent external validation cohorts.

GSE185263, the training cohort, generated by the GPL16791 high-throughput sequencing platform, consists of 348 septic and 44 control samples (17). The GRCh38 Human Genome Assembly (ncbi.nlm.nih.gov/datasets/genome/GCF_000001405.40/) was downloaded, the raw counts of the RNA-sequencing dataset were annotated and the data were normalized as transcripts per kilobase million (18).

The three other microarray datasets, GSE57065, GSE131761 and GSE95233, were annotated by matching series matrices and corresponding annotation files, and the data were uniformly normalized using robust multiarray averaging, with log2 transformation. GSE57065, the test cohort, generated by the GPL570 microarray platform, included 82 septic and 25 control samples (19), whereas GSE131761 (validation cohort A), generated by the GPL13497 microarray platform, contained 81 septic and 15 control samples (20) and GSE95233 (validation cohort B), generated by the GPL570 microarray platform, comprised 102 septic and 22 control samples (21).

Differentially expressed gene (DEG) analysis. In the training cohort, DEGs were screened using the R package 'edgeR' version 4.6.2 (bioconductor.org/packages/release/bioc/html/edgeR.html) with a threshold of |log fold change|≥1 and a false discovery rate <0.05 (22). DEGs were then visualized using the R packages 'ggplot2' and 'pheatmap'.

Enrichment analyses. Gene Ontology (GO) and Kyoto Encyclopedia of Genes and Genomes (KEGG) enrichment analyses of DEGs were performed using the R package 'clusterProfiler' (23); gene set variation analysis (GSVA) was performed to reveal the status of signaling pathways between groups using the R packages 'GSVA' (24) and 'DOSE' (25).

All results were filtered through a threshold of P≤0.05, and data were visualized using the R package 'enrichplot'.

FRDEG screening. In the present study, FRDEGs were defined as the overlapping genes of DEGs and ferroptosis-related genes (FRGs). The latter were separately obtained from the FerrDb database (26) (n=484) and the GeneCards database (27) (n=92), genes with a relevance score >3 were retained. After combining the two lists of FRGs, duplicated genes were removed and a set of unique FRGs (n=506) was generated. The intersection of DEGs and FRGs was visualized using the R package 'ggvenn' and the intersecting genes were identified as FRDEGs.

PPIN construction. PPINs have been applied to identify key regulators in biological processes (28). In the present study, a PPIN was used to identify key regulators in sepsis-associated ferroptosis, and these key regulators were defined as hub-FRDEGs. To build the PPIN, FRDEGs were imported into the Search Tool for the Retrieval of Interacting Genes/Proteins (STRING) online database (29), the PPINs were then imported into Cytoscape (30) for visualization.

To select hub-FRDEGs from the raw PPIN, 'cytoHubba', a Cytoscape plugin for network ranking, was deployed in order to rank the topological importance of each PPIN node using different algorithms (31). In the present study, five CytoHubba algorithms, Maximum Neighborhood Component, Density of Maximum Neighborhood Component, Maximal Clique Centrality, Edge Percolated Component and Degree, were used to rank the PPIN nodes, and the top 50 nodes from each algorithm were chosen, intersected and pinpointed as hub FRDEGs. In addition, chromosomal locations of hub FRDEGs were recognized and portrayed using the R package 'RCicos'.

Machine learning analysis. Machine learning algorithms enable the number of candidate hub-FRDEGs to be reduced using the modelling fitting of the transcriptomic profile. Conforming to specific key parameters, the hub-FRDEGs selected by the machine learning algorithms were deemed to be the hub-FRDEGs that were most relevant to sepsis. In the present study, three machine learning algorithms, namely the least absolute shrinkage and selection operator (LASSO), support vector machine-recursive feature elimination (SVM-RFE) and random forest, were used to select the hub-FRDEGs that were most relevant to sepsis.

For the LASSO algorithm, the key parameter was the λ value determining the binomial deviance of model fitting, and the λ value responding to the minimum binomial deviance was deemed as optimal (32). Under the optimal λ, all hub-FRDEGs retained in the LASSO fitting model were selected using the R package 'glmnet' (33). Regarding the random forest algorithm, the key parameter was the Gini index, and all hub-FRDEGs were rated and selected below the specific Gini index using the R package 'randomForest' (34). Considering the SVM-RFE algorithm, realized using the R package 'e1071', all the hub-FRDEGs that minimized the 10-fold cross-validation error rate were recommended (35). Overlapping hub-FRDEGs, as selected by the algorithms, were deemed to be the hub-FRDEGs for further study, and their closeness with other genes was analyzed and visualized using the GeneMANIA database (36).

Logistic regression and nomogram construction. In the training cohort, logistic regression analysis was performed to build a predictive model of sepsis using the R package 'rms'. A diagnostic nomogram was subsequently constructed according to the logistic regression formula, and its diagnostic accuracy was evaluated using the calibration curve, the confusion matrix, the decision curve and the receiver operating characteristic (ROC) curve. The differences in expression were then identified by comparing the hub-FRDEGs between the control and sepsis samples, and these were subsequently visualized using heatmaps and box-plots, whereas their diagnostic accuracy was assessed using the ROC curve. The calibration curve with Homer-Lemeshow test, decision curve, heatmap, ROC curve and box plots were constructed using the R packages 'caret', 'rmda', 'pheatmap', 'pROC' and 'ggplot2', respectively. Finally, the confusion matrix was calculated using the R package 'caret', and subsequently visualized for presentation.

To validate the diagnostic accuracy of the hub-FRDEGs and nomogram, the changes in expression of hub-FRDEGs under septic conditions were quantified, the area under the curve (AUC) values in the ROC curves of the hub-FRDEGs and nomogram were calculated, and all results in the test cohort (GSE57065), validation cohort A (GSE131761) and validation cohort B (GSE95233) were visualized. The changes in hub-FRDEGs resulting from sepsis were visualized using box plots and heatmaps, whereas the diagnostic accuracies of hub-FRDEGs and nomograms were visualized using a confusion matrix and calibration curve, respectively.

Ferroptotic clustering of septic samples. Consensus clustering analysis revealed the distinct ferroptotic patterns of sepsis samples using the R package 'ConsesusClusterPlus'. According to the change in area under the cumulative distribution function curve, the optimal number of clusters (with k ranging from 2-10) was determined, and septic samples were classified based on the expression level of the ferroptotic gene signature. Principal component analysis (PCA) of septic clusters was subsequently performed to reveal the disparities in the septic data using the R package 'factoextra'. The transcriptomic differences of the hub-FRDEGs between clusters were subsequently evaluated and visualized using box plots and heatmaps. The immunocyte abundance between septic clusters was measured after analyzing the immune microenvironment in all the samples. DEGs between septic subgroups were screened using the R package 'edgeR', and enrichment analyses (GO and KEGG) were then performed to reveal their metabolic differences.

Immune microenvironment analysis. In the training cohort, 22 types of immune cellular components and degrees were measured using the R package 'CIBERSORT' (37). Septic changes of the immunocytes were calculated and visualized using box plots, and the correlation between immunocyte abundance and the hub FRDEG transcriptomic profile was quantified and plotted. The correlation between infiltrating immunocytes was also measured using Pearson's correlation coefficient and visualized using the R package 'corrplot'. Furthermore, the infiltration score of 28 immunocytes (38) was computed using single-sample gene set enrichment analysis (ssGSEA). The ssGSEA algorithm was used to calculate the

proportion of immunocytes using the R-package 'GSVA' (24) and the metagene list of 28 immunocytes (38). Results were expressed in the form of an infiltration score between 0 and 1. The ssGSEA algorithm and CIBERSORT were often revealed to be mutually complementary to each other with respect to evaluating the immune infiltration (39-41). Using the ssGSEA algorithm, the immune cell proportions comparing between samples that exhibited a differential expression of hub-FRDEGs were compared and visualized.

Cell culture and treatment. All reagents and resources used in the present study are presented in Table SI. The human monocyte cell line THP-1 was obtained from Wuhan Pricella Biotechnology Co., Ltd ., and the cells were cultured in RPMI-1640 medium containing 10% fetal bovine serum and 0.05 mM β-mercaptoethanol in an incubator at 37˚C in an atmosphere containing 5% CO_2.

THP-1 cells were treated with 100 nM phorbol myristate acetate (PMA) for 24 h to induce their differentiation into macrophage-like cells at 37˚C. The treated cells were further cultured in medium without PMA for 24 h to enable them to stabilize and mature into M0 macrophages (42) at 37˚C. To simulate the sepsis microenvironment, lipopolysaccharide (LPS; 1 μg/ml) was added following the induction of THP 1 differentiation, and the incubation was allowed to continue for 24 h at 37˚C (43).

Reverse transcription-quantitative polymerase chain reaction (RT-qPCR) assay. Total RNA was isolated from $2.5x10^6$ adherent cells using TRIzol® reagent (cat. no. 15596026; Invitrogen; Thermo Fisher Scientific, Inc.). and reverse-transcribed into cDNA using PrimeScript™ RT reagent Kit with gDNA Eraser (Takara, catalog number RR047A) at 37˚C for 15 min), step 2 (85˚C at 5 sec), and step 3 (4˚C). SYBR Green qPCR Master Mix solution (MedChemExpress, catalog number HY-K0501), was used for PCR following the manufacturer's instructions.

Primers were obtained from the Beijing Tsingke Biotech Co., Ltd.. RT-qPCR analysis was performed using a CFX96 Touch Real-Time PCR Detection System (C1000Touch™; Bio-Rad Laboratories, Inc.). Thermocycling conditions were as follows: Initial denaturation at 95˚C for 30 sec, followed by 40 cycles of 5 sec at 95˚C and 30-60 sec at 60˚C. ACTB (β-actin) was amplified as the internal reference gene. The $2^{-\Delta\Delta Cq}$ method was applied for quantification of the data (44).

Western blot analysis. Cells were lysed in RIPA lysis buffer containing PMSF, protease and phosphatase inhibitor cocktail for 30 min at 4˚C, and then centrifuged at 12,000 x g for 15 min in 4˚C. The protein supernatant was concentrated, and the protein concentration was measured using a BCA protein assay kit. Subsequently, 10% SDS-PAGE electrophoresis was used to separate 10 μl protein samples at the concentration of 2 μg/μl. Subsequently, the gels containing the separated proteins were cut horizontally according to the corresponding molecular weights of the protein, and the gel slices were transferred to polyvinylidene fluoride membranes, followed by blocking with 5% skimmed milk for 1 h at room temperature. The membranes were incubated overnight at 4˚C with primary antibodies (1:1,000 dilution; diluted according to the instructions of the manufacturer). The membranes were then incubated with horseradish peroxidase-conjugated secondary anti-rabbit or anti-mouse IgG (1:10,000 dilution) for 1 h at room temperature. Finally, the levels of the proteins were detected using a chemiluminescence reagent kit, and the protein expression density was quantified using Quantity One Software (Bio-Rad Laboratories, Inc.).

Small interfering (si)RNA transfection. Thioredoxin (TXN)-targeting siRNA (si-TXN; 5'-UUUGACUUCACA CUCUGAAGC-3') or non-targeting control siRNA (si-NC; 5'-CCUACGCCACCAAUUUCGU-3') were synthesized by the Beijing Tsingke Biotech Co., Ltd. Induced $1.5x10^6$ M_0 macrophage cells in the exponential growth phase were seeded into 6-well plates. These cells were subsequently transiently transfected with either 10 μl si-TXN or si-NC (100 nmol/l) using Advanced Transfection Reagent (Zeta Life, cat. no. AD600150). The duration of transfection was 24 h at 37˚C, and the duration between the end of transfection and subsequent experiments was 24 h.

Malondialdehyde (MDA) assay. MDA content was measured following the manufacturer's protocol. In brief, fresh THP-1-derived macrophages were collected and lysed on ice for 20 min to prepare samples. After the MDA solution was added to each sample or standard, the mixture was heated at 100˚C for 15 min and subsequently centrifuged at 1,000 x g for 10 min to harvest the supernatant at 4˚C. The absorbance of the supernatant was then measured at optical density (OD)= 532 nm using a colorimetric method, and MDA levels were expressed as nmol/mg.

Determination of reduced glutathione (GSH)/oxidized glutathione (GSSG) activity. GSH/GSSG detection was performed according to the manufacturer's instructions. Briefly, fresh THP-1-derived macrophages were collected. Each sample was divided into two aliquots: One for measuring the GSSG content following treatment with the GSH clearing reagent, and the other for measuring the total GSH content without treatment. The OD values were measured at 412 nm using a Multiskan™ FC Microplate Photometer (cat. no. 51119100; Thermo Fisher Scientific, Inc.), and the contents of total GSH, GSSG and reduced GSH were calculated.

Measurement of Fe^{2+} levels. Fe^{2+} levels were evaluated using the FerroOrange staining method. After removing the previous culture medium, the cells were washed twice in a serum-free RPMI-1640 medium. A working solution of 1 μmol/l FerroOrange fluorescent probe was prepared in a serum-free RPMI-1640 medium before being added to the cells. The cells were incubated at 37˚C in a dark environment for 30 min. Subsequently, the nuclei were labelled with Hoechst 33342. The cells were then observed and images were captured using a Leica DMi8 fluorescence microscope. Finally, the fluorescence intensity due to FerroOrange staining was quantified using ImageJ software version 1.54m (National Institutes of Health).

Statistical analysis. The bioinformatical data obtained from the various analyses underwent statistical evaluation using R software (version 4.2.2). The Shapiro-Wilk test was deployed to assess the normality of the data, and the unpaired Student's t-test or Wilcoxon rank sum test was used to compare the

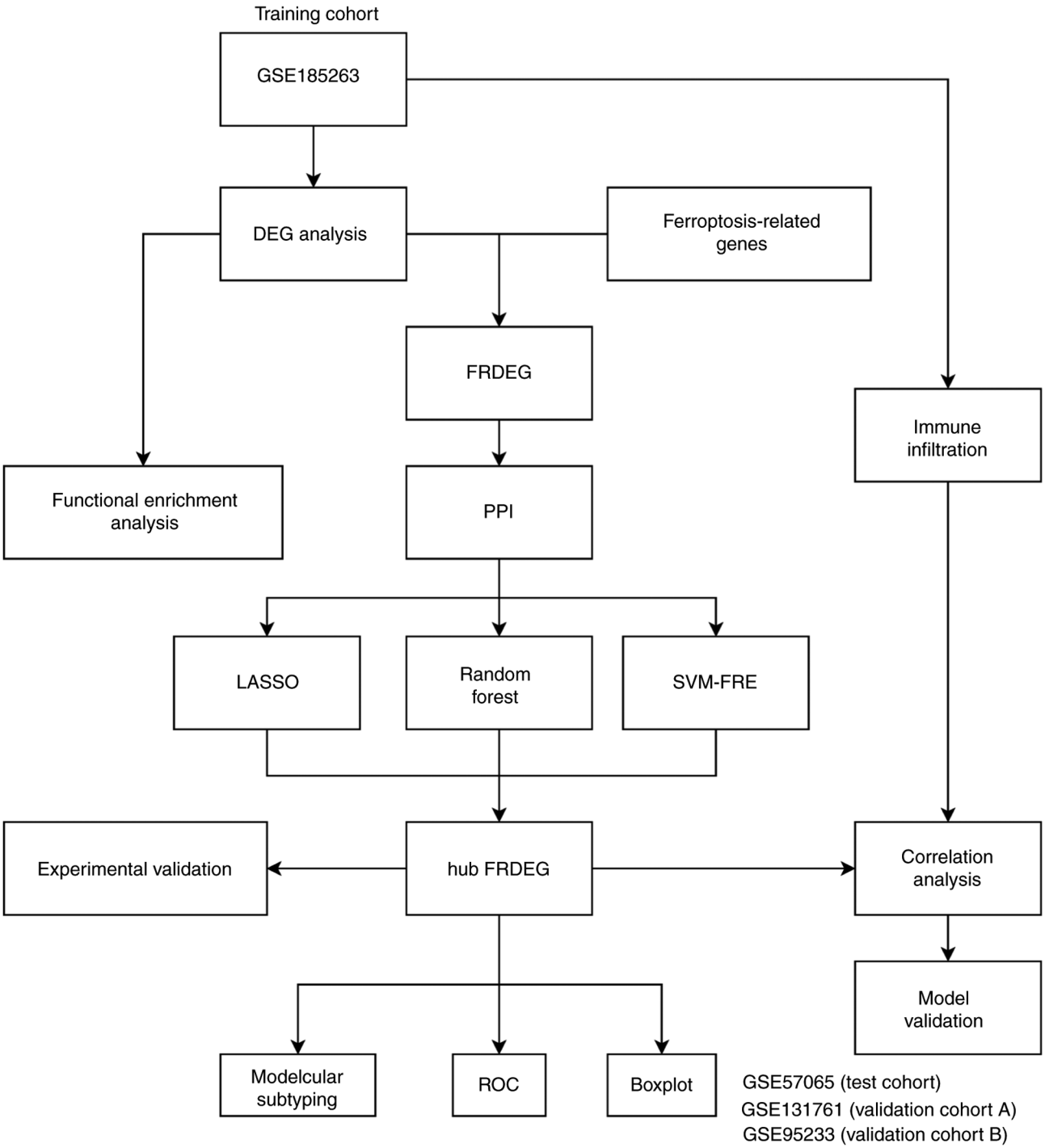

Figure 1. Flow chart of the study. FRDEG, ferroptosis-related differentially expression genes; PPI, protein-protein interaction; LASSO, least absolute shrinkage and selection operator; SVM-FRE, support vector machine recursive feature elimination; ROC, receiver operating characteristic.

differences in transcriptomics and immune infiltration. Comparisons between multiple groups were made by one-way analysis of variance, followed by the Bonferroni post hoc test. Data analysis and the construction of graphs were performed using GraphPad Prism 10 (Dotmatics). $P<0.05$ was considered to indicate a statistically significant difference.

Results

Identification of FRDEGs between the control and sepsis groups. The overall design of the present study is presented in Fig. 1. Datasets acquired are summarized in Table I. A total of 4,410 DEGs between the sepsis and control groups were obtained from the training cohort (Table SII). The Volcano plot (Fig. 2A) and heatmap (Fig. 2B) reveal the transcriptomic distribution of DEGs. FRGs (n=506; Table SIII) were obtained and aggregated from the FerrDb and GeneCards database (Fig. 2C), and overlapping genes (n=94; Fig. 2D) between the DEGs (n=4,410) and FRGs were identified as FRDEGs for the subsequent analytic steps.

Selection of hub-FRDEGs. FRDEGs were loaded into the STRING database in order to construct the PPIN, and

Table I. Datasets acquired for the present study.

Dataset	Platform	Species	Tissue	Type	Sample size	Number of control samples	Number of sepsis samples
GSE185263	GPL16791	Homo sapiens	Whole blood	High-throughput sequencing	392	44	348
GSE57065	GPL570	Homo sapiens	Whole blood	Microarray	107	25	82
GSE131761	GPL13497	Homo sapiens	Whole blood	Microarray	96	15	81
GSE95233	GPL570	Homo sapiens	Whole blood	Microarray	124	22	102

hub-FRDEGs (n=84) were selected as the nodes (Fig. 2E). Hub-FRDEGs were ranked according to five internal algorithms of CytoHubba in the Cytoscape desktop utility, and the top 50 hub-FRDEGs from diverse rankings were then intersected (Table SIV and Fig. 2F). Shared hub-FRDEGs (n=38) were identified as candidates for determining machine learning algorithms, and their chromosomal positions are shown in Fig. 2G. LASSO was employed as the machine learning algorithm, and 18 hub-FRDEGs were selected for the minimum binomial deviance (Table SV; Fig. 3A and B); upon employing random forest, three hub-FRDEGs below the cut-off Gini of 6 were selected (Table SVI; Fig. 3C-D); upon using SVM-RFE, the lowest 10-fold error rate was attained when considering 38 of the hub-FRDEGs (Table SVII and Fig. 3E). Intersection among the three machine learning algorithms determined the hub-FRDEGs (n=3) that were most relevant to sepsis, namely ataxia telangiectasia mutated (ATM), dipeptidyl peptidase 4 (DPP4) and TXN (Fig. 3F), with the predicted interaction network shown in Fig. 3G.

Construction, visualization and validation of diagnostic model. In the training cohort, a binary logistic model was purposed for classifying the status of patients into either of the control or sepsis groups according to the ATM, DPP4 and TXN expression levels. The logistic formula applied was as follows: Logit (P=Sepsis) =0.2244-(0.0704 x ATM expression levels)+(0.0755 x TXN expression levels)-(0.0840 x DPP4 expression levels). The diagnostic nomogram was subsequently plotted (Fig. 4A). The decision curve revealed the acceptable clinical utility of this nomogram to be 0-1 when predicting the septic status (Fig. 4B).

The transcriptomic septic changes of the hub-FRDEGs were initially examined in the training cohort (Fig. 4C and Table SVIII), the test cohort (Fig. 4D and Table SIX), validation cohort A (Fig. 4E and Table SIX) and validation cohort B (Fig. 4F and Table SIX), which revealed that the expression levels of both ATM and DPP4 were significantly decreased in the sepsis group when compared with control. TXN also revealed a transcriptomic elevation when examining the septic status. Subsequently, the ROC curves of biomarkers and the nomogram in the training cohort, test cohort, validation cohort A and validation cohort B showed the diagnostic accuracy of both hub-FRDEGs and nomogram was high in all cohorts(Fig. 4G-J), and these data are summarized in Table II. Furthermore, the confusion matrix of this nomogram in the training cohort (Fig. 4K) revealed that the model had an acceptable specificity (65.91%), high sensitivity (98.56%) and high diagnostic accuracy (94.90%), and the confusion matrix of this nomogram in the test cohort, validation cohort A and validation cohort B (Fig. 4L-N) revealed comparable or elevated values for the specificity, sensitivity and accuracy. Moreover, the unsupervised hierarchical clustering of the three hub-FRDEGs revealed their strength in distinguishing septic from control status (Fig. 4O); in addition, their strong performance in classifying sepsis in the test cohort, validation cohort A and validation cohort B was also confirmed (Fig. 4P and R). Finally, the calibration curve of the nomogram in the training cohort was drawn with the P-value of the Homer-Lemeshow test >0.05, which revealed a satisfactory performance in modelling fitness (Fig. 4S); parallel fitness of this diagnostic logistic model was also demonstrated by the calibration curve in the test cohort, validation cohort A and validation cohort B (Fig. 4T-V).

Enrichment analyses of dysfunctional signaling pathways. GO functional enrichment analysis of DEGs from the training cohort consists of biological process (BP), cellular component (CC) and molecular function (MF) categories (Table SX and Fig. 5A and B). The BP category included processes such as the 'production of molecular mediators of the immune response', 'humoral immune response' and 'immunoglobulin production'. The CC category contained processes such as the 'immunoglobulin complex', the 'external side of the plasma membrane' and the 'immunoglobulin complex, circulating'. Finally, the MF category featured processes such as 'antigen binding, 'immunoglobulin receptor binding' and 'structural constituents of chromatin'. KEGG pathway enrichment analysis of the DEGs mainly revealed processes such as 'neutrophil extracellular trap formation', 'systemic lupus erythematosus', transcriptional mis-regulation in cancer' and 'alcoholism' (Table SXI and Fig. 5C and D). The results from GSVA revealed that septic progression primarily activates inflammatory and metabolic signaling pathways, including 'cysteine-type endopeptidase inhibitor activity', 'antimicrobial humoral immune response mediated by an antimicrobial peptide', 'fatty acid binding', 'defense response to fungus' and 'endopeptidase regulator activity', and cellular axes such as tissue morphogenesis and transformation were found to be deactivated, including 'embryonic appendage morphogenesis', 'lung saccule development', 'regulation of animal organ morphogenesis' and 'negative regulation of vascular-associated smooth muscle cell differentiation' (Table SXII and Fig. 5E).

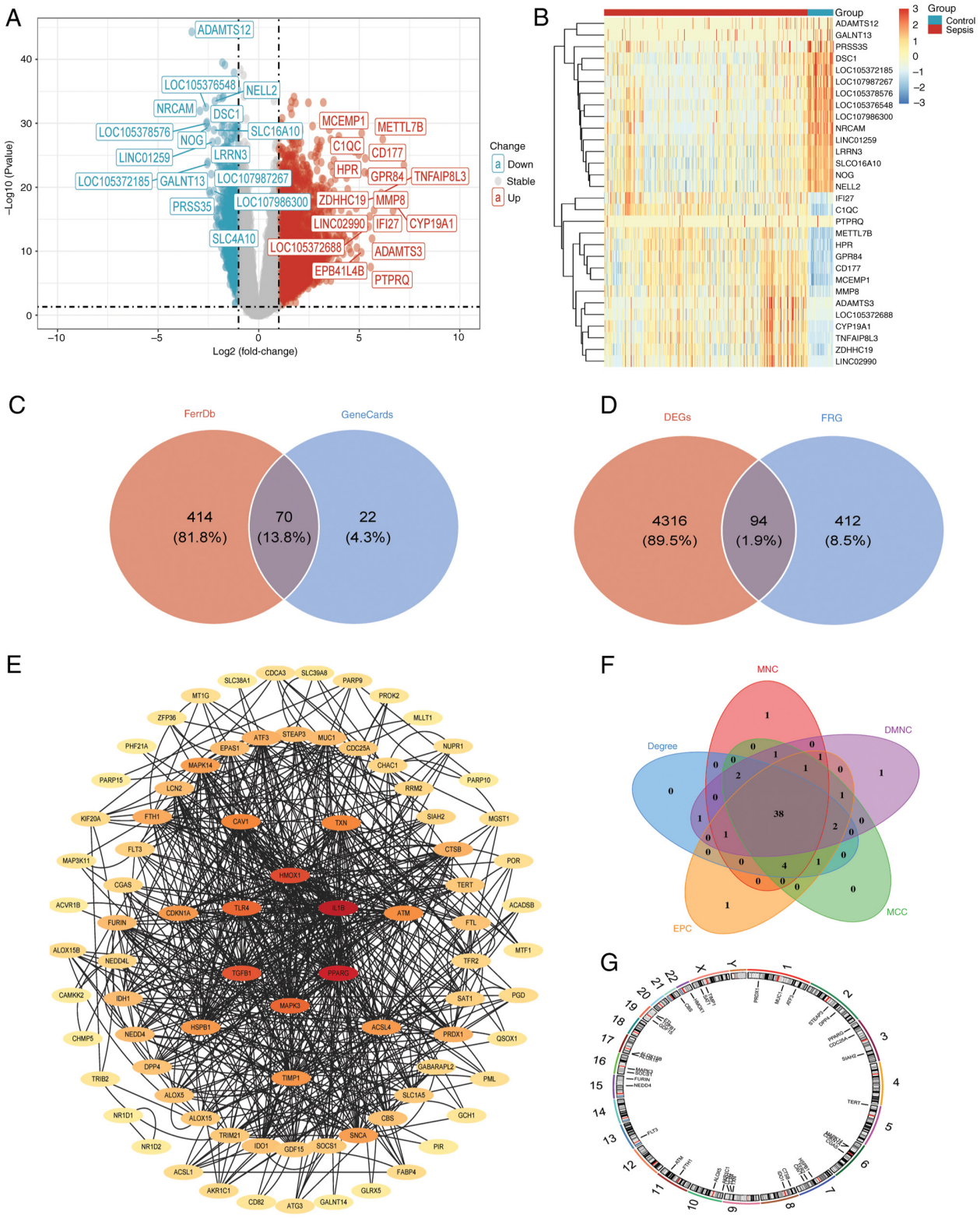

Figure 2. Screening of hub ferroptosis-related DEGs. (A) Volcano plot of DEGs. (B) Heatmap of top 15 upregulated and downregulated DEGs. (C) FRGs collected from FerrDb and GeneCards. (D) Venn diagram of DEGs and FRGs for attaining FRDEGs. (E) Protein-protein interaction network by the Search Tool for the Retrieval of Interacting Genes/Proteins database. (F) Venn diagram of multiple ranking algorithms for hub-FRDEGs. (G) Chromosomal locations of hub-FRDEGs. DEG, differentially expressed genes; MNC, maximum neighborhood component; DMNC, density of maximum neighborhood component; MCC, maximal clique centrality; EPC, edge percolated component; FRGs, ferroptosis-related genes; FRDEGs, ferroptosis-related differential expression genes.

Consensus clustering distinguished two ferroptotic septic patterns. Using the transcriptomic profile of three hub-FRDEGs as a suitable base, two distinct septic patterns were identified by consensus clustering, which were termed cluster A and cluster B (Table SXIII and Fig. 6A-D). A PCA plot of the septic clusters revealed their ferroptotic disparity

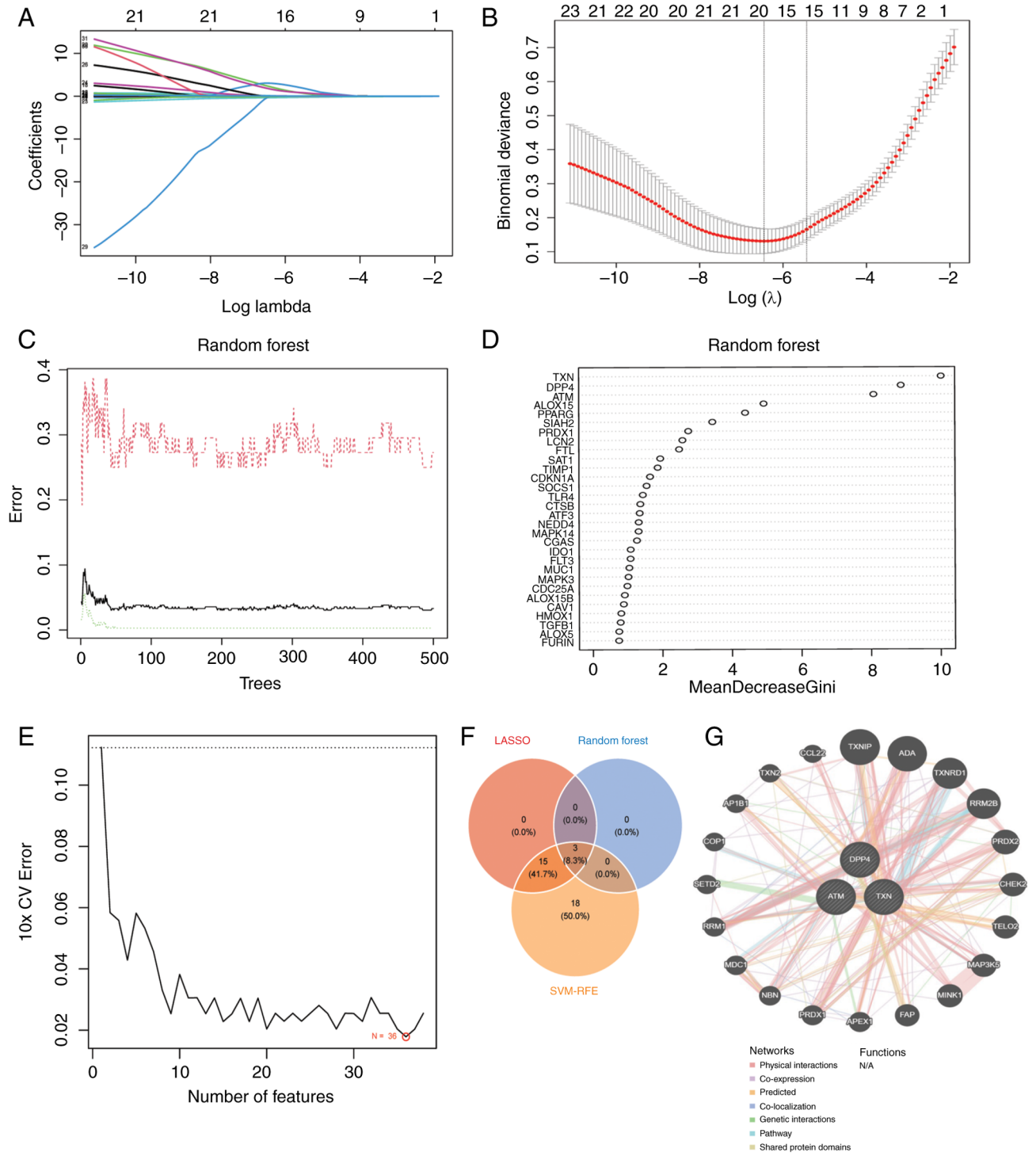

Figure 3. Selection of candidate hub-FRDEGs by machine learning. (A) LASSO selection operator model. (B) Cross-validation for tuning the parameter selection in the LASSO regression. (C) Correlation between the number of trees and model error in the random forest algorithm. (D) Results obtained by Gini coefficient method in the random forest algorithm. (E) SVM-RFE algorithms. (F) Venn diagram of multiple machine learning algorithms. (G) Interaction network of three hub-FRDEGs (ATM, DPP4 and TXN) and their predicted genes with predicted weight percentages using GeneMANIA. FRDEGs, ferroptosis-related differential expression genes; CV, cross validation; LASSO, least absolute shrinkage and selection operator algorithms; SVM-RFE, support vector machine recursive feature elimination algorithms; ATM, ataxia telangiectasia mutated; DDP4, dipeptidyl peptidase 4; TXN, thioredoxin.

(Fig. 6E). Compared with cluster A, the TXN and ATM expression levels were reduced in cluster B, and DPP4 revealed a comparable distinction between the clusters (Fig. 6F and G). After the subsequent analysis of the septic immune microenvironment, the abundance of 22 immunocytes between the two clusters was discerned using CIBERSORT (Fig. 6H). Analysis revealed ~50% of the immunocytes were differentially distributed, including M_0 macrophages, $CD4^+$ memory resting T Cells, γδT Cells, regulatory T Cells (Tregs), monocytes, resting natural killer (NK) cells and neutrophils. Differential expression analysis of the clusters was subsequently performed, followed by GO and KEGG enrichment analyses.

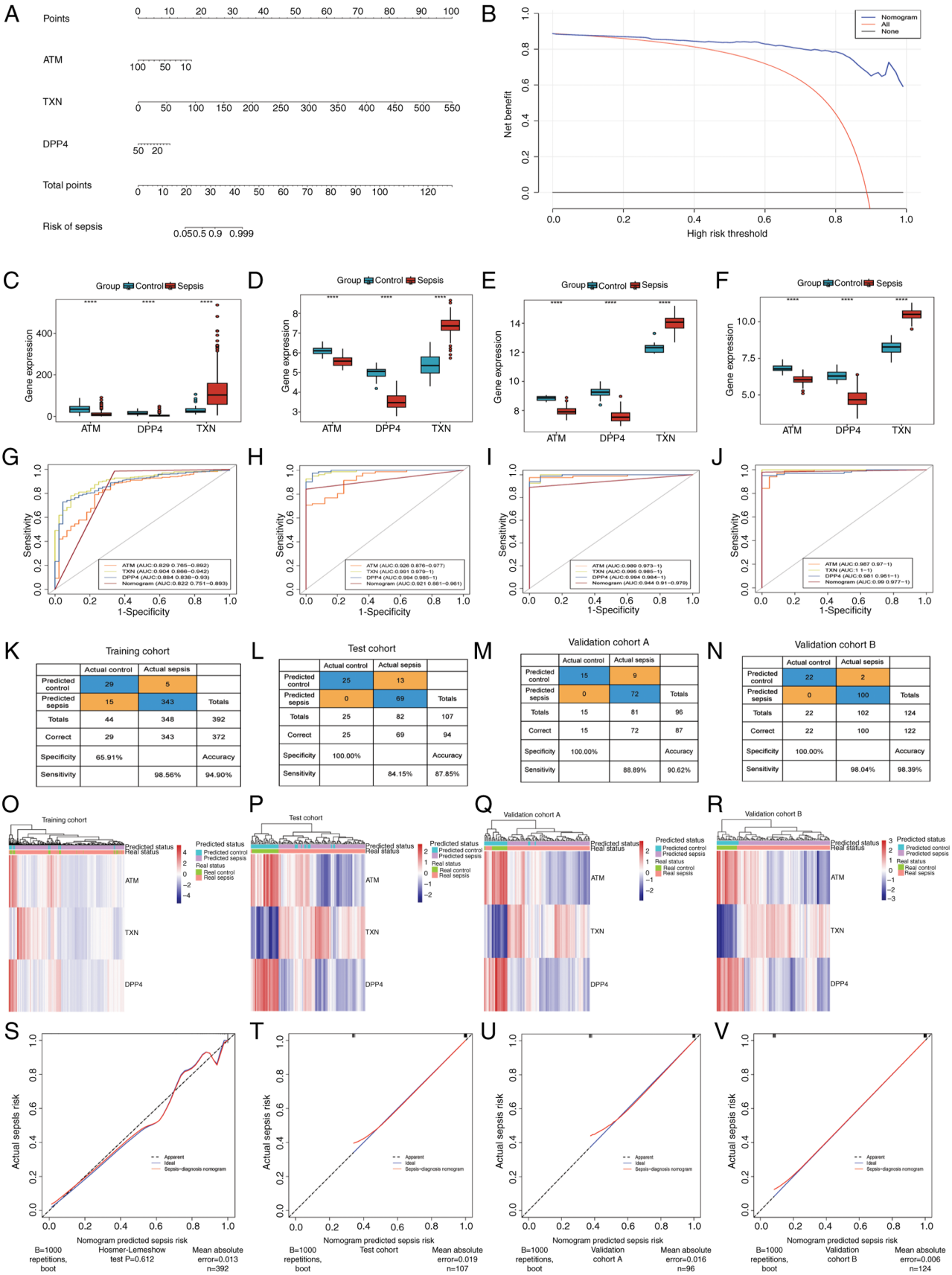

Figure 4. Ferroptotic septic prediction model. (A) Nomogram for predicting the risk of sepsis by the ferroptotic panel. (B) Decision curve of the nomogram on the training cohort. Boxplot of ATM, DPP4 and TXN on the (C) training cohort, (D) test cohort, (E) validation cohort A and (F) validation cohort B. ROC curves of ATM, TXN, DPP4, and the nomogram on the (G) training cohort, (H) test cohort, (I) validation cohort A and (J) validation cohort B. Confusion matrix of model on the (K) training cohort, (L) test cohort, (M) validation cohort A (N) and validation cohort B. Unsupervised clustering heatmap of ATM, TXN, and DPP4 on the (O) training cohort, (P) test cohort, (Q) validation cohort A and (R) validation cohort B. Calibration curve of nomogram on (S) training cohort, (T) test cohort, (U) validation cohort A and (V) validation cohort B. ****P<0.0001, respectively. ATM, ataxia telangiectasia mutated; DDP4, dipeptidyl peptidase 4; TXN, thioredoxin.

Table II. The AUC of biomarkers and nomogram's ROC curve with 95%CI.

Gene	Training cohort (95% CI)	Test cohort (95% CI)	Validation cohort A (95% CI)	Validation cohort B (95% CI)
ATM	0.828 (0.765-0.892)	0.926 (0.876-0.977)	0.989 (0.973-1.000)	0.987 (0.971-1.000)
DPP4	0.884 (0.838-0.930)	0.994 (0.985-1.000)	0.994 (0.984-1.000)	0.981 (0.961-1.000)
TXN	0.904 (0.866-0.942)	0.991 (0.980-1.000)	0.995 (0.985-1.000)	1.000 (1.000-1.000)
Nomogram	0.822 (0.751-0.894)	0.920 (0.881-0.961)	0.944 (0.910-0.979)	0.990 (0.977-1.000)

Table III. Primer sequences in real-time quantitative polymerase chain reaction detection

Gene in Homo sapiens	Forward primer sequences (5' to 3')	Reverse primer sequences (5' to 3')
ATM	CCAGGCAGGAATCATTCAG	CAATCCTTTTAAATAGACGGAAAGAA
DPP4	AGTGGCACGGCAACACAT	AGAGCTTCTATCCCGATGACTT
TXN	ATGAAAGAAAGGCTTGATCATTTTGC	TAAACTTGTAGTAGTTGACTTCTCAGC
ACTB	GGCACCACACCTTCTACAATGAG	GGATAGCACAGCCTGGATAGCA

GO enrichment analysis of the clusters revealed that the BP category mainly contained 'immunoglobulin production', 'complement activation, classical pathway'; the CC category predominantly included 'immunoglobulin complex', 'immunoglobulin complex, circulating' and 'hemoglobin complex'; and the MF category included processes such as 'antigen binding', 'immunoglobulin receptor binding' and 'haptoglobin binding' (Fig. 6I). By contrast, KEGG enrichment analysis of the clusters only revealed an association with the 'malaria' pathway (Fig. 6J).

Immune microenvironment analysis of sepsis. Septic changes of the immune microenvironment were investigated using the CIBERSORT and ssGSEA algorithms, respectively. Initially, the quantitative differences of the 22 immunocytes between the control and sepsis groups were analyzed (Table SXIV; Fig. 7A and B). The majority of the immunocytes were revealed to be septically modulated, as exemplified by the aggravated infiltration of neutrophils, monocytes and M_0 macrophages, and the sepsis-induced decreases in the populations of $CD4^+$ memory resting T Cells, $CD8^+$ T Cells and resting NK cells. The correlation between the transcriptomics of the hub-FRDEGs and the abundance of immunocytes was subsequently visualized by heatmap analysis (Fig. 7C). Both ATM and DPP4 were revealed to be positively associated with $CD4^+$ memory resting T Cells, $CD8^+$ T Cells, resting NK cells and naive B cells. TXN was negatively correlated with neutrophils, T follicular helper cells, M_0 macrophages and γδT Cells. The correlation between immunocytes was also visualized(Fig. 7D) . Furthermore, the immune scores comparing between samples with differential expression of hub-FRDEGs were compared using ssGSEA (Table SXV and Fig. 7E-G). Samples with a high expression of ATM were revealed to have increased infiltrated levels of activated B cells, activated $CD4^+$ T Cells and activated $CD8^+$ T Cells, although the opposite findings were obtained for activated dendritic cells, macrophages, monocytes and type 2 T helper cells (Fig. 7E). Similar results were observed in samples with high expression of DPP4, except for monocytes and type 2 T helper cells (Fig. 7F). However, samples with high expression of TXN exhibited reduced proportions of activated $CD8^+$ T Cells, $CD56^+$ NK cells, $CD4^+$ central memory T Cells and $CD8^+$ effector memory T Cells, whereas the oppose degree of infiltration was observed for activated $CD4^+$ T Cells and γδT Cells (Fig. 7G).

Validation of hub genes in the in vitro model. To validate the expression of key genes in sepsis-induced ferroptosis, THP-1-derived macrophages were treated with LPS for 24 h to mimic this process and to establish an *in vitro* model. Findings of RT-qPCR and western blotting data were consistent with those of the bioinformatics data analysis. Primer sequences are presented in Table III. Compared with the control group, the relative mRNA expression levels of DDP4 (Fig. 8A) and ATM (Fig. 8B) were significantly decreased, whereas that of TXN (Fig. 8C) increased in the model group when compared with control. The results of the western blotting experiments revealed that, compared with the control group, the expression levels of ATM and DPP4 protein in the model group were significantly decreased, whereas that of TXN was increased (Fig. 8D and E).

TXN inhibition is able to augment ferroptosis in macrophages following sepsis. TXN is a key antioxidant and regulator of ferroptosis (45). TXN was demonstrated to alleviate ferroptosis by the upregulation of GPX4 in a mouse model of Parkinson's disease (46), and has been identified as a hub ferroptotic regulator of proliferative diabetic retinopathy (47). Furthermore, TXN has been identified as the downstream target of retinoic acid receptor α, and as an inhibitor of ferroptosis in lung adenocarcinoma (48). The present study revealed that the AUC value of TXN was the highest among the ROC curves constructed for the three hub-FRDEGs. Therefore, TXN was

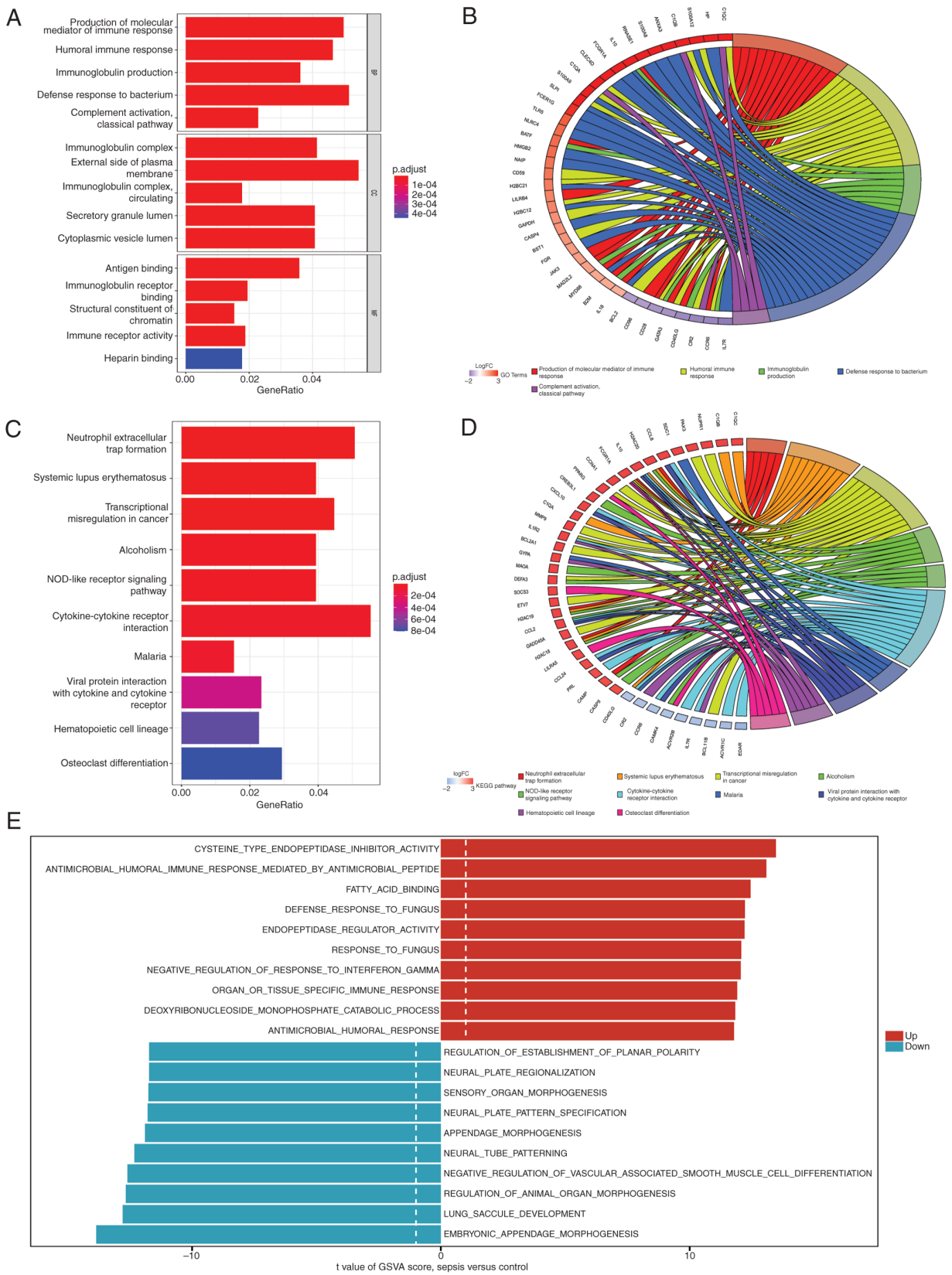

Figure 5. Functional enrichment analysis. (A) GO enrichment analysis. (B) GO enrichment analysis chord diagram. (C) KEGG enrichment analysis. (D) KEGG enrichment analysis chord diagram. (E) GSVA Enrichment Analysis. GO, gene ontology; KEGG, Kyoto Encyclopedia of Genes and Genomes; GSVA, gene set variation analysis.

further investigated to validate these findings. Reduced TXN expression was revealed in samples treated with si-TXN when compared with control (Fig. 8F-G). Ferroptosis-associated markers in TXN-inhibited and control macrophages were examined following LPS treatment. Western blotting experiments revealed significantly reduced expression levels of the

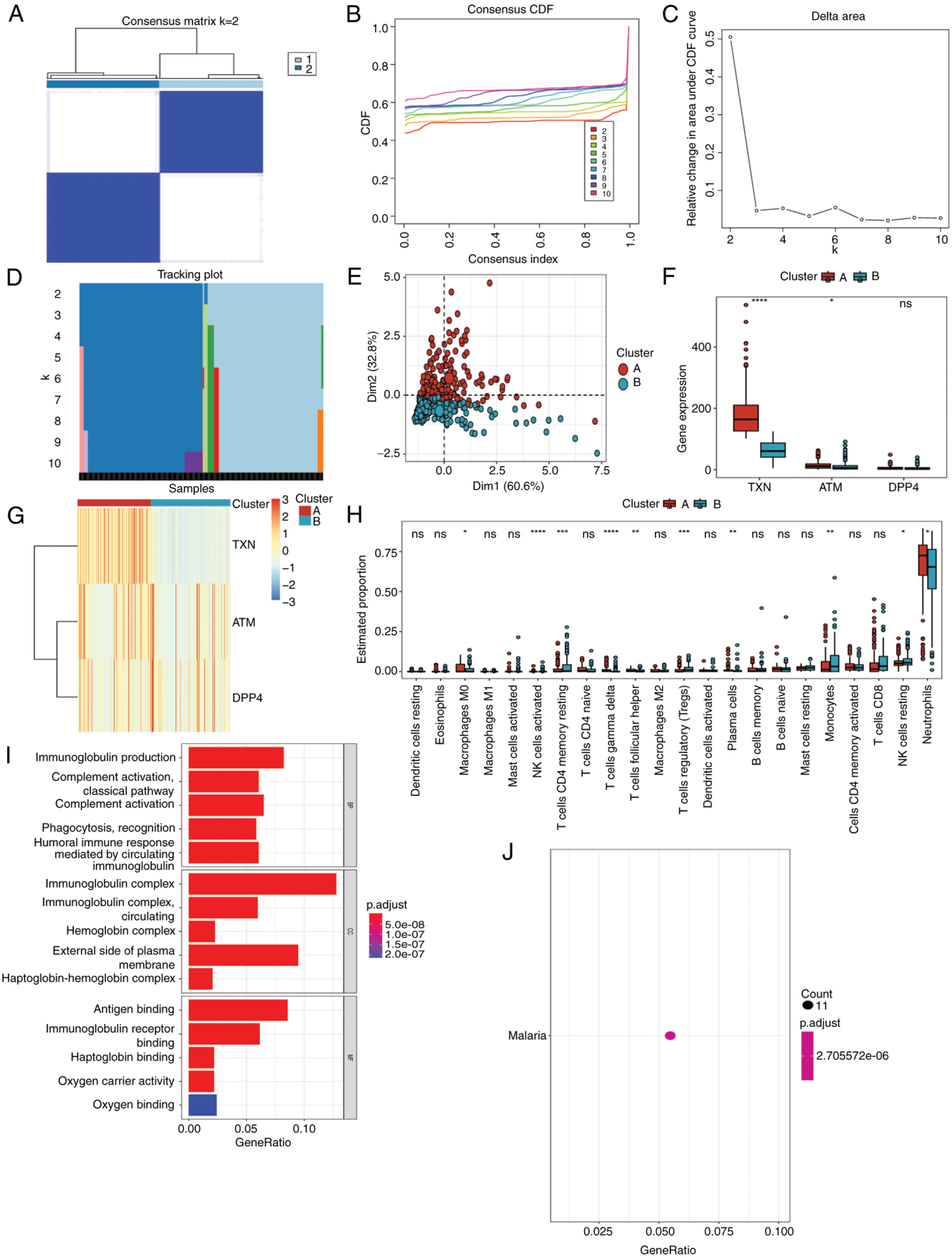

Figure 6. Distinct ferroptotic patterns of sepsis. (A) Consensus matrix (k=2). (B) Consensus CDF curve. (C) δ area curve. (D) Tracking plot. (E) Principal component analysis plot of two clusters. (F) Boxplot of TXN, ATM and DPP4 between clusters. (G) Heatmap of TXN, ATM and DPP4 between clusters. (H) Comparison of the abundance of 22 immunocytes between two clusters. (I) Gene Ontology enrichment analysis of clusters. (J) Kyoto Encyclopedia of Genes and Genomes enrichment analysis of clusters. *P<0.05, **P<0.01, ***P<0.001 and ****P<0.0001, respectively. CDF, cumulative distribution function; ATM, ataxia telangiectasia mutated; DDP4, dipeptidyl peptidase 4; TXN, thioredoxin. Dim, dimension; ns, not significant.

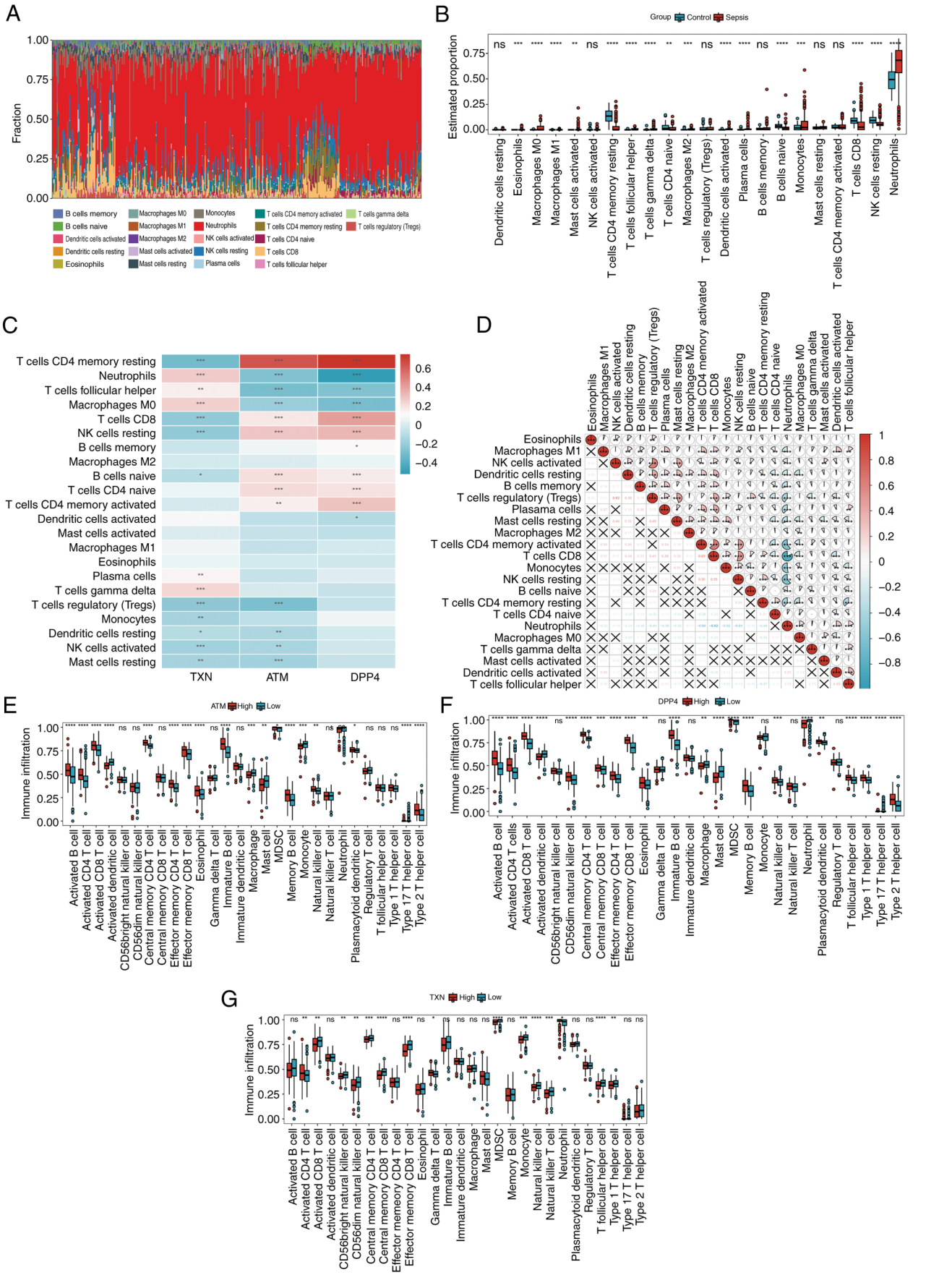

Figure 7. Immune microenvironment analysis. (A) Stack plot of 22 immunocytes distribution in the training cohort. (B) Comparison of the abundance of 22 immunocytes between control group and sepsis group. (C) Correlation between TXN, ATM and DPP4 and 22 immunocytes. (D) Correlation between 22 immunocytes. Immune microenvironment in groups with differential expression of (E) ATM, (F) DPP4 and (G) TXN using single sample gene set enrichment analysis. *P<0.05, **P<0.01, ***P<0.001 and ****P<0.0001, respectively. ATM, ataxia telangiectasia mutated; DDP4, dipeptidyl peptidase 4; TXN, thioredoxin.

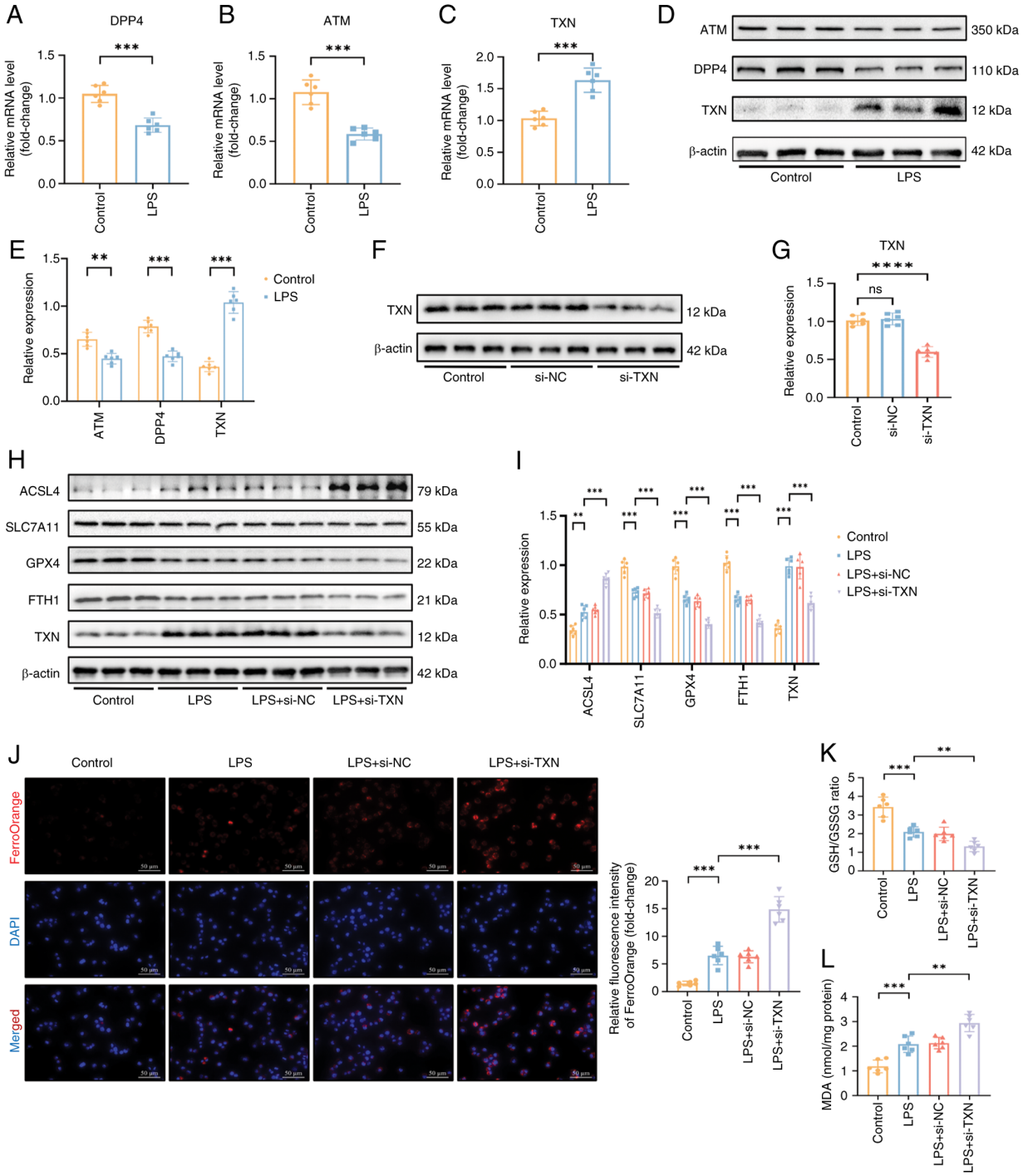

Figure 8. Validation of hub genes in the *in vitro* model. Quantification of mRNA expression levels of hub-FRDEGs (A) DPP4, (B) ATM and (C) TXN in THP-1-derived macrophages in control and LPS-treated model group, ACTB was used as an internal reference gene. (D) Representative western blotting images of hub-FRDEGs and β-actin in control and model group. (E) Semi-quantitative analysis of hub-FRDEGs was performed. (F) Representative western blotting images of TXN and β-actin in control group, si-NC group, and si-TXN group. (G) Semi-quantitative analysis of TXN was performed. (H) Representative western blotting images of ferroptosis-related biomarkers (ACSL4, SLC7A11, GPX4, FTH1), TXN and β-actin in control group, LPS group, LPS+si-NC group and LPS+si-TXN group. (I) Semi-quantitative analysis of ACSL4, SLC7A11, GPX4, FTH1 and TXN was performed. (J) Representative images of FerroOrange staining (red, FerroOrange-positive staining; blue, Hoechst 33342) in each group. Characteristic biological changes of ferroptosis in TXN inhibited and non-inhibited macrophages after LPS exposure are (K) GSH/GSSG (L) MDA. Scale bar, 50 μm. Relative fluorescence intensity was quantified using ImageJ. n=6 per group. Data are shown as the mean ± SD. **P<0.01, ***P<0.001, and ****P<0.0001 respectively. ATM, ataxia telangiectasia mutated; DDP4, dipeptidyl peptidase 4; TXN, thioredoxin; LPS; si, small interfering; NC, negative control; ACSL4, acyl-CoA synthetase long-chain family member 4; SLC7A11, solute carrier family 7 member 11; GPX4, glutathione peroxidase 4; FTH1, ferritin heavy chain 1; GSH, glutathione; GSSG, oxidized glutathione; MDA; malondialdehyde; FRDEGs, ferroptosis-related differential expression genes.

proteins solute carrier family 7 member 11, GPX4 and ferritin heavy chain 1, which act as defenders against ferroptosis, in the LPS group compared with the control group. Compared with the si-NC+LPS and LPS groups, their expression was further decreased in the si-TNX+LPS group, compared with the LPS only treated group. Furthermore, the level of the

lipid peroxidation-promoting protein ACSL4 was increased following LPS treatment compared with control, and treatment with si-TXN led to a further elevation of its expression level when compared with LPS only treated group (Fig. 8H and I). The FerroOrange staining experiments further suggested that LPS treatment caused an increase in Fe^{2+} levels in macrophages, and subsequent treatment with si-TXN augmented this increase (Fig. 8J). Treatment with LPS led to a decrease in the GSH/GSSG ratio of macrophages compared with control, and subsequent si-TXN treatment caused a further decrease in this ratio compared with LPS only treated samples (Fig. 8K). In addition, the MDA detection experiments suggested that treatment with LPS led to an increase in the lipid peroxidation level of the macrophages compared with control, and subsequent si-TXN treatment caused a further increase compared with the LPS only treated group (Fig. 8L). Taken together, these results reveal that treatment of the cells with TXN resulted in an increased level of ferroptosis in macrophages following sepsis.

Discussion

Sepsis invokes inflammatory dysfunction and subsequently, fatal multi-organ dysfunction (49). In addition, the outcomes of sepsis management programs, at present, are unsatisfactory, as characterized by the high mortality rates of patients with sepsis (It is associated with a mortality rate of 10-20%) (50), highlighting the urgent need for rapid diagnosis and effective therapies (49). However, the majority of the known septic biomarkers lack sufficient and independent validation, and a comprehensive diagnosis comprising biomarker assessment combined with clinical evaluation would be expected to improve sepsis management (51). Moreover, the overall role of inflammation in sepsis is complicated as it has a dual role in hyper-inflammation and immuno-suppression (50), and further work to elucidate a complete understanding of the mechanisms underlying the role of inflammation in sepsis.

Ferroptosis is a type of programmed cell death, mainly comprising iron metabolism disturbance, lipid peroxidation and collapse of the antioxidant system (52). Inflammatory signaling pathways may initially trigger ferroptosis (6). Inflammation combined with ferroptosis has been demonstrated to result in extensive septic organ damage (53). Sepsis-induced cardiac injury was revealed to be rescued by blocking ferroptosis (54), and targeting ferroptosis was revealed to alleviate the septic damage induced in the lung (55), kidney (56) and brain (57). Nevertheless, the network of ferroptosis regulation in sepsis requires further investigation to enable ferroptosis to be effectively targeted for clinical utility.

Overall, in building the ferroptotic diagnostic model, the present study has examined transcriptomic profiles through differential expression analysis, constructing the PPIN and the employment of three machine learning algorithms, resulting in the identification of ATM, DPP4 and TXN. Their diagnostic value was evaluated from both separate and holistic perspectives. Moreover, enrichment analyses were performed, which suggested that a hyper-activation of the immune response and inhibition of tissue morphogenesis and transformation were involved in the process. Furthermore, disparities of the septic patterns according to the three-panel ferroptosis signature were investigated, revealing their distinct features when facing septic challenges. Finally, the identified septic changes of the three hub-FRDEGs were validated *in vitro*, which demonstrated that TXN rescued macrophages from ferroptosis under conditions of LPS-induced sepsis.

Ferroptotic associations among the three hub FRDEGs (namely, ATM, DPP4 and TXN) and sepsis were disclosed in the present study. ATM has been revealed to function as a key sensor of DNA damage responses, and as a redox sensor (58,59). ATM also has a role in maintaining iron homeostasis (60), and was demonstrated to mediate the ATM-nuclear receptor coactivator 4 (NCOA4) ferroptotic signaling pathway induced by deoxynivalenol (61,62). The regulation of iron metabolism mediated by ATM is especially noteworthy. ATM was revealed to be sensitive to changes in the concentration of (chelated) iron (63). In another study, compared with wild-type mice, ATM-deficient mice exhibited increased labile iron levels (64), and a different study, revealed that a tendency to accumulate iron was associated with a marked increase in hepatic oxidative stress (65). ATM inhibition alleviates ferroptosis by activating iron regulators that are responsible for iron storage and export (60). The transcriptomic levels of ATM were also revealed to be considerably reduced in pediatric sepsis (66), and a similar trend was observed in heart tissue derived from a LPS-induced animal model (67), findings that are consistent with the results of the present study.

The association between DPP4 and ferroptosis, however, remains poorly understood. Tumor suppressor p53 was demonstrated to invoke ferroptosis by facilitating DDP4 nuclear localization, and DPP4 has been identified as a novel diagnostic marker of inflammatory diseases such as atherosclerosis (68) and ulcerative colitis (69). Septic changes and the targeting of DPP4 have disclosed its therapeutic potential. DPP4 was revealed to be markedly reduced in leukocytes obtained from patients with sepsis (70). In the present study, the septic changes of DPP4 were investigated bioinformatically, and subsequently validated experimentally. However, the clinical application of DPP4 remains a challenge in terms of the currently available methods of sepsis management. Compared with patients treated with sodium-glucose cotransporter 2 (SGLT2) as an inhibitor, both hospital admissions due to sepsis and the mortality rate increased in those administered DPP4 as an inhibitor (71,72). An investigation of the TXN redox system upon treatment with TXN revealed an eradication of oxidative stress levels and a sustainment of the redox balance (68). TXN was revealed to interrupt ferroptosis through activating GPX4, and overexpression of TXN reversed the effects of knocking down retinoic acid receptor-α on ferroptosis both *in vitro* and *in vivo* (48). TXN was identified as a ferroptosis-associated biomarker in proliferative diabetic retinopathy (47) and its septic role was disclosed in the perspective of studies undertaken on the endoplasmic reticulum (73) and PANoptosis (namely, a novel inflammatory cell death mechanism that combines features of pyroptosis, apoptosis and necroptosis) (74). The present study showed that TXN may influence the development of sepsis by regulating ferroptosis, as an innovative insights about the role of TXN in sepsis. Additionally, the diagnostic accuracy of ATM, DPP4 and TXN was also demonstrated, and the AUC values of their ROC curves demonstrated their potential role as separate septic classifiers in all cohorts.

Although TXN was investigated for further validation, similar septic findings regarding ATM and DPP4 are noteworthy. ATM was downregulated in the septic status, and it was identified as a cellular senescence-associated key gene both in sepsis and sepsis-induced acute respiratory distress syndrome (75). It was also recognized as a key immune-related gene of pediatric sepsis (66). ATM was revealed to mitigate the LPS-induced disruption of the blood-brain barrier by regulating mitochondrial homeostasis (76), and it was indispensable for the anthracyclines-induced protection against severe sepsis by regulating DNA damage response (77). However, the level of DPP4 also decreased in septic shock with moderate diagnostic accuracy (AUC =0.86) (78). DPP4 was identified as one core therapeutic target in sepsis (79), and its septic association with ferroptosis was also demonstrated (70). DPP4 inhibitors initially demonstrated their therapeutic effect on sepsis. DPP4 inhibitors aggravated the risk of hospital admission for infection (odd ratio=1.04) (80), and targeting DPP4 during sepsis-induced hyper-procalcitonemia significantly reduced capillary leakage by 60.4±6.9% (81). In endotoxemic mice, the DPP4 inhibitor linagliptin alleviated endothelial inflammation (82), improved microvascular function (83) and demonstrated therapeutic effects comparable to DPP4 knockout (84). Linagliptin alleviated LPS-induced acute lung injury by preserving the pulmonary microvascular barrier (85) and improved the survival of the CLP-induced rat (86). However, the future of DPP4-oriented therapy for sepsis remains controversial. Compared with patients prescribed DPP4 inhibitors, sodium-glucose cotransporter 2 inhibitors were considerably associated with a lower risk of sepsis-related mortality (hazard ratio=0.39) (72). Both septic admissions and septic mortality were significantly reduced in SGLT2 inhibitor users compared with DPP4 inhibitor users [admissions for sepsis: 45 [0.4%] vs. 134 [0.8%]; and mortality: 59 [0.6%] vs. 414 (2.3%], respectively) (71). Glucagon-like peptide-1 receptor-deficient endotoxemic mice were also insensitive to linagliptin and liraglutide (87). Due to the detailed dissection of the roles of ATM and DPP4 and the lack of previous studies investigating the role of TXN in sepsis, TXN was selected as the target of further investigation.

To the best of our knowledge, the present study is the first to have built and validated a septic diagnostic nomogram based entirely on the novel ATM-DPP4-TXN ferroptotic signature using logistic regression analysis and multiple external validations. Previous studies have mainly focused on the prognostic model of sepsis from the perspective of ferroptosis (88-90). These models were mainly based on the combination of several clinical variables and one or two ferroptotic biomarker(s); for example, ribonucleotide reductase M2 and ribosomal protein L7A (89), Lipin-1 (88) or Alox5 (90). In constructing ferroptotic diagnostic models of sepsis, one study proposed a seven-panel ferroptotic diagnostic model, reporting an AUC value of 1.000 without visual nomogram and external validations (91). Another study established a two-panel ferroptotic diagnostic model using the 'XGBoost' classifier, which included high AUC values, both with the training cohort (AUC=0.711) and two validation cohorts (AUC=0.961 and 0.913) (16). Compared with these two models, the model created in the present study may offer a more promising option for clinical septic diagnosis using a smaller panel of ferroptotic biomarkers, since this model was constructed as one three-panel ferroptotic diagnostic model of sepsis, using logistic regression, which demonstrated comparable AUC values with the training cohort (AUC=0.822) and multiple external validations (test cohort, AUC=0.921; validation cohort A, AUC=0.944; and validation cohort B, AUC=0.99).

Nevertheless, there remain unresolved problems in the application of this nomogram. First, the model lacked the validation of diverse populations. The model was constructed using only the transcriptomic profile of three genes; other clinical variables (for example, age, sex and comorbidity) should be also integrated for accurate diagnosis. In addition, given the medical laws that protect the privacy of patients, electronic records which could provide clinical variables are essentially inadmissible. Secondly, the samples in the present study were collected from whole blood, which requires RT-qPCR analysis in the clinic; because of the rapid progression and high mortality rates of sepsis, the time required to carry out routine RT-qPCR of hub-FRDEGs and subsequent model diagnosis could seriously delay both the diagnosis and treatment of sepsis. The feasibility of conducting RT-qPCR analysis should be balanced against the availability of time for evaluation and treatment. Finally, the application of this diagnostic model was limited to the septic classification, which would not be applicable to samples originating from septic organ damage. There are certain lethal septic complications that require rapid diagnosis and treatment, including sepsis-induced acute lung injury, septic cardiomyopathy and sepsis-induced acute respiratory distress syndrome. The model created in the present study was essentially constructed on samples from patients with sepsis/septic shock and control patients, and further training and validation would be required for other septic complications. Future working will include collecting the matching clinical information of patients with sepsis for validation of diverse populations, combining the transcriptomic profiles of the hub-FRDEGs with more accessible clinical variables in order to assess balancing the feasibility of treatment with the time that would be required for the therapy, and to complement the samples with those featuring other septic complications in order to broaden the diagnostic application.

The present study identified two septic patterns and their heterogeneity was assessed in terms of hub-FRDEG expression and the signaling pathway status, which revealed two distinct and identifiable septic traits from the perspective of ferroptosis. In brief, the clinical utility of three hub-FRDEGs was investigated from the perspective of differential diagnosis and their septic traits, and their ferroptotic roles in terms of controlling sepsis have been initially disclosed in the present study.

Also associated with septic ferroptosis in relation to the hub-FRDEGs that were investigated in the present study is dysfunction in the immune microenvironment. In the present study, both ATM and DPP4 were revealed to be associated with the proliferation of $CD4^+$ memory resting T Cells, activated $CD4^+$ T Cells, activated $CD8^+$ T Cells and effector memory $CD8^+$ T Cells. TXN exerted an inhibitory effect on

these inflammatory phenomena, also promoting a marked infiltration of neutrophils. From the onset of sepsis, marked reductions in the numbers of $CD4^+$ T Cells were observed, and their participatory roles in cytokine production and immunogenic proliferation were severely restricted (92). Similarly, the population of circulating $CD8^+$ memory cells was temporarily compromised, and this disturbance was observed to continue during septic progression (93). Ferroptosis is associated with inflammation, and therefore the role of ferroptosis-mediated immune responses is pivotal in terms of the progression of sepsis (8). The ferroptotic death of $CD4^+$ T Cells was previously reported in the onset of sepsis caused by severe polytrauma (94). A close association of GPX4 with naive $CD4^+$ and $CD8^+$ T Cells and Tregs in pediatric sepsis has also been reported (95). NCOA4, a ferroptotic regulator, was revealed to aggravate septic inflammatory responses by interacting with the stimulator of interferon response cGAMP interactor 1 in macrophages (96). However, further investigations are required to improve understanding of the septic context of the ferroptosis-mediated immune response. In this regard, the present study has increased the knowledge of the role of ferroptosis in septic inflammation from the perspective of analyzing three hub-FRDEGs and monitoring the changes in T Cells, and targeting T Cells may offer a promising avenue for treating sepsis in the future.

Numerous limitations are associated with the present study. For example, all samples from datasets were derived from the blood and septic changes of these three hub-FRDEGs in other tissues were not examined. Given that rescuing critical patients is an emergency, collecting blood samples was determined to be the most convenient method for potentially providing new options for septic diagnosis and management. Septic samples derived from additional tissues will be investigated in future studies.

Additionally, the specific mechanism underlying how the three hub-FRDEGs regulate the septic immune microenvironment has yet to be fully elucidated. Due to the complexity of the regulatory network of these hub-FRDEGs, future studies should investigate their associated machinery to help explain the exact septic implications.

In conclusion, the present study performed a bioinformatics analysis of septic changes at the transcriptomic level, thereby identifying three hub-FRDEGs (ATM, DPP4 and TXN) as a future basis for septic diagnosis and management. The diagnostic accuracies of the three hub-FRDEGs were examined separately, and then translated into one diagnostic nomogram, with excellent performance and external validation. Septic dysfunction in the immune microenvironment, as determined from the aberrant infiltration of immune cells, was also associated with ferroptosis in connection with the hub-FRDEGs. Moreover, two distinct ferroptotic septic patterns were recognized and analyzed, demonstrating the challenges presented by heterogeneity. Future investigations will mainly focus on hub-FRDEG-induced pharmacological interventions against sepsis, with the intention of delving deeper into the intricate mechanisms underlying ferroptosis-associated sepsis.

Acknowledgements

Not applicable.

Funding

The present study was supported by the Chongqing Graduate Scientific Research Innovation Project (grant no. CYS23326).

Availability of data and materials

The data generated in the present study are included in the figures and/or tables of this article.

Authors' contributions

MW, ZZ, YP, and SL performed experiments. YP and SL interpreted data. MW and ZZ wrote the manuscript, contributed to the design of the study. YP and SL were involved in the conception and design of the study and contributed substantially to revising the manuscript for important intellectual content. MW, ZZ and SL confirm the authenticity of all the raw data. All authors have read and approved the final manuscript.

Ethics approval

Not applicable.

Patient consent for publication

Not applicable.

Competing interests

The authors declare that they have no competing interests.

References

1. Rudd KE, Johnson SC, Agesa KM, Shackelford KA, Tsoi D, Kievlan DR, Colombara DV, Ikuta KS, Kissoon N, Finfer S, *et al*: Global, regional, and national sepsis incidence and mortality, 1990-2017: Analysis for the global burden of disease study. Lancet 395: 200-211, 2020.
2. Kamath S, Hammad Altaq H and Abdo T: Management of sepsis and septic shock: What have we learned in the last two decades? Microorganisms 11: 2231, 2023.
3. Póvoa P, Coelho L, Dal-Pizzol F, Ferrer R, Huttner A, Conway Morris A, Nobre V, Ramirez P, Rouze A, Salluh J, *et al*: How to use biomarkers of infection or sepsis at the bedside: Guide to clinicians. Intensive Care Med 49: 142-153, 2023.
4. Pierrakos C, Velissaris D, Bisdorff M, Marshall JC and Vincent JL: Biomarkers of sepsis: Time for a reappraisal. Crit Care 24: 287, 2020.
5. Liang D, Minikes AM and Jiang X: Ferroptosis at the intersection of lipid metabolism and cellular signaling. Mol Cell 82: 2215-2227, 2022.
6. Chen Y, Fang ZM, Yi X, Wei X and Jiang DS: The interaction between ferroptosis and inflammatory signaling pathways. Cell Death Dis 14: 205, 2023.
7. Sun Y, Chen P, Zhai B, Zhang M, Xiang Y, Fang J, Xu S, Gao Y, Chen X, Sui X and Li G: The emerging role of ferroptosis in inflammation. Biomed Pharmacother 127: 110108, 2020.
8. Huo L, Liu C, Yuan Y, Liu X and Cao Q: Pharmacological inhibition of ferroptosis as a therapeutic target for sepsis-associated organ damage. Eur J Med Chem 257: 115438, 2023.
9. Zhang H, Liu J, Zhou Y, Qu M, Wang Y, Guo K, Shen R, Sun Z, Cata JP, Yang S, *et al*: Neutrophil extracellular traps mediate m^6A modification and regulates sepsis-associated acute lung injury by activating ferroptosis in alveolar epithelial cells. Int J Biol Sci 18: 3337-3357, 2022.

10. Xiao Z, Zhang J, Qiu Z, Liu H, Ding H, Li H, Liu Y, Zou X and Long J: Ferroptosis and inflammation are modulated by the NFIL3-ACSL4 axis in sepsis associated-acute kidney injury. Cell Death Discov 10: 349, 2024.
11. Chen J, Feng M, Zhang T, Zhong M, Wang Y, Zhang Q and Sun Y: Integrative bioinformatics analysis reveals CGAS as a ferroptosis-related signature gene in sepsis and screens the potential natural inhibitors of CGAS. Int J Biol Macromol 297: 139778, 2025.
12. Leek JT, Scharpf RB, Bravo HC, Simcha D, Langmead B, Johnson WE, Geman D, Baggerly K and Irizarry RA: Tackling the widespread and critical impact of batch effects in high-throughput data. Nat Rev Genet 11: 733-739, 2010.
13. Hoyle DC, Rattray M, Jupp R and Brass A: Making sense of microarray data distributions. Bioinformatics 18: 576-584, 2002.
14. Newman AM, Liu CL, Green MR, Gentles AJ, Feng W, Xu Y, Hoang CD, Diehn M and Alizadeh AA: Robust enumeration of cell subsets from tissue expression profiles. Nat Methods 12: 453-457, 2015.
15. Bradford JR, Hey Y, Yates T, Li Y, Pepper SD and Miller CJ: A comparison of massively parallel nucleotide sequencing with oligonucleotide microarrays for global transcription profiling. BMC Genomics 11: 282, 2010.
16. Chen Z, Wei S, Yuan Z, Chang R, Chen X, Fu Y and Wu W: Machine learning reveals ferroptosis features and a novel ferroptosis classifier in patients with sepsis. Immun Inflamm Dis 12: e1279, 2024.
17. Baghela A, Pena OM, Lee AH, Baquir B, Falsafi R, An A, Farmer SW, Hurlburt A, Mondragon-Cardona A, Rivera JD, *et al*: Predicting sepsis severity at first clinical presentation: The role of endotypes and mechanistic signatures. EBioMedicine 75: 103776, 2022.
18. Zhao S, Ye Z and Stanton R: Misuse of RPKM or TPM normalization when comparing across samples and sequencing protocols. RNA 26: 903-909, 2020.
19. Tabone O, Mommert M, Jourdan C, Cerrato E, Legrand M, Lepape A, Allaouchiche B, Rimmelé T, Pachot A, Monneret G, *et al*: Endogenous retroviruses transcriptional modulation after severe infection, trauma and burn. Front Immunol 9: 3091, 2019.
20. Martínez-Paz P, Aragón-Camino M, Gómez-Sánchez E, Lorenzo-López M, Gómez-Pesquera E, Fadrique-Fuentes A, Liu P, Tamayo-Velasco Á, Ortega-Loubon C, Martín-Fernández M, *et al*: Distinguishing septic shock from non-septic shock in postsurgical patients using gene expression. J Infect 83: 147-155, 2021.
21. Venet F, Schilling J, Cazalis MA, Demaret J, Poujol F, Girardot T, Rouget C, Pachot A, Lepape A, Friggeri A, *et al*: Modulation of LILRB2 protein and mRNA expressions in septic shock patients and after ex vivo lipopolysaccharide stimulation. Hum Immunol 78: 441-450, 2017.
22. Robinson MD, McCarthy DJ and Smyth GK: edgeR: A Bioconductor package for differential expression analysis of digital gene expression data. Bioinformatics 26: 139-140, 2010.
23. Wu T, Hu E, Xu S, Chen M, Guo P, Dai Z, Feng T, Zhou L, Tang W, Zhan L, *et al*: clusterProfiler 4.0: A universal enrichment tool for interpreting omics data. Innovation (Camb) 2: 100141, 2021.
24. Hänzelmann S, Castelo R and Guinney J: GSVA: Gene set variation analysis for microarray and RNA-seq data. BMC Bioinformatics 14: 7, 2013.
25. Yu G, Wang LG, Yan GR and He QY: DOSE: An R/Bioconductor package for disease ontology semantic and enrichment analysis. Bioinformatics 31: 608-609, 2015.
26. Zhou N, Yuan X, Du Q, Zhang Z, Shi X, Bao J, Ning Y and Peng L: FerrDb V2: Update of the manually curated database of ferroptosis regulators and ferroptosis-disease associations. Nucleic Acids Res 51: D571-D582, 2023.
27. Stelzer G, Rosen N, Plaschkes I, Zimmerman S, Twik M, Fishilevich S, Stein TI, Nudel R, Lieder I, Mazor Y, *et al*: The genecards suite: From gene data mining to disease genome sequence analyses. Curr Protoc Bioinformatics 54: 1.30.31-31.30.33, 2016.
28. Farooq QUA, Shaukat Z, Aiman S and Li CH: Protein-protein interactions: Methods, databases, and applications in virus-host study. World J Virol 10: 288-300, 2021.
29. Szklarczyk D, Kirsch R, Koutrouli M, Nastou K, Mehryary F, Hachilif R, Gable AL, Fang T, Doncheva NT, Pyysalo S, *et al*: The STRING database in 2023: Protein-protein association networks and functional enrichment analyses for any sequenced genome of interest. Nucleic Acids Res 51: D638-D646, 2023.
30. Doncheva NT, Morris JH, Gorodkin J and Jensen LJ: Cytoscape stringApp: Network analysis and visualization of proteomics data. J Proteome Res 18: 623-632, 2019.
31. Chin CH, Chen SH, Wu HH, Ho CW, Ko MT and Lin CY: cytoHubba: Identifying hub objects and sub-networks from complex interactome. BMC Syst Biol 8 Suppl 4 (Suppl 4): S11, 2014.
32. Bühlmann P and Geer S: Statistics for high-dimensional data: Method, Theory and Applications. Springer Berlin, Heidelberg, 2011.
33. Friedman J, Hastie T and Tibshirani R: Regularization paths for generalized linear models via coordinate descent. J Stat Softw 33: 1-22, 2010.
34. Breiman L: Random forests. Machine Learning 45: 5-32, 2001.
35. Sanz H, Valim C, Vegas E, Oller JM and Reverter F: SVM-RFE: Selection and visualization of the most relevant features through non-linear kernels. BMC Bioinformatics 19: 432, 2018.
36. Warde-Farley D, Donaldson SL, Comes O, Zuberi K, Badrawi R, Chao P, Franz M, Grouios C, Kazi F, Lopes CT, *et al*: The GeneMANIA prediction server: Biological network integration for gene prioritization and predicting gene function. Nucleic Acids Res 38: W214-220, 2010.
37. Chen B, Khodadoust MS, Liu CL, Newman AM and Alizadeh AA: Profiling tumor infiltrating immune cells with CIBERSORT. Methods Mol Biol 1711: 243-259, 2018.
38. Charoentong P, Finotello F, Angelova M, Mayer C, Efremova M, Rieder D, Hackl H and Trajanoski Z: Pan-cancer immunogenomic analyses reveal genotype-immunophenotype relationships and predictors of response to checkpoint blockade. Cell Rep 18: 248-262, 2017.
39. Liu G, Wang M, Lv X, Guan Y, Li J and Xie J: Identification of mitochondria-related gene biomarkers associated with immune infiltration in acute myocardial infarction. iScience 27: 110275, 2024.
40. Xue H, Xiao Z, Zhao X, Li S, Wang Z, Zhao J and Zhu F: A comprehensive analysis of immune features and construction of an immune gene diagnostic model for sepsis. BMC Genomics 24: 794, 2023.
41. Zhang Y, Ma X, Liu C, Bie Z, Liu G, Liu P and Yang Z: Identification of HSPD1 as a novel invasive biomarker associated with mitophagy in pituitary adenomas. Transl Oncol 41: 101886, 2024.
42. Baxter EW, Graham AE, Re NA, Carr IM, Robinson JI, Mackie SL and Morgan AW: Standardized protocols for differentiation of THP-1 cells to macrophages with distinct M(IFNγ+LPS), M(IL-4) and M(IL-10) phenotypes. J Immunol Methods 478: 112721, 2020.
43. Xu W, Wu Y, Wang S, Hu S, Wang Y, Zhou W, Chen Y, Li Q, Zhu L, Yang H and Lv X: Melatonin alleviates septic ARDS by inhibiting NCOA4-mediated ferritinophagy in alveolar macrophages. Cell Death Discov 10: 253, 2024.
44. Livak KJ and Schmittgen TD: Analysis of relative gene expression data using real-time quantitative PCR and the 2(-Delta Delta C(T)) method. Methods 25: 402-408, 2001.
45. Llabani E, Hicklin RW, Lee HY, Motika SE, Crawford LA, Weerapana E and Hergenrother PJ: Diverse compounds from pleuromutilin lead to a thioredoxin inhibitor and inducer of ferroptosis. Nat Chem 11: 521-532, 2019.
46. Bai L, Yan F, Deng R, Gu R, Zhang X and Bai J: Thioredoxin-1 rescues MPP(+)/MPTP-induced ferroptosis by increasing glutathione peroxidase 4. Mol Neurobiol 58: 3187-3197, 2021.
47. Cao D, Wang C and Zhou L: Identification and comprehensive analysis of ferroptosis-related genes as potential biomarkers for the diagnosis and treatment of proliferative diabetic retinopathy by bioinformatics methods. Exp Eye Res 232: 109513, 2023.
48. Bian Y, Shan G, Liang J, Hu Z, Sui Q, Shi H, Wang Q, Bi G and Zhan C: Retinoic acid receptor alpha inhibits ferroptosis by promoting thioredoxin and protein phosphatase 1F in lung adenocarcinoma. Commun Biol 7: 751, 2024.
49. Singer M, Deutschman CS, Seymour CW, Shankar-Hari M, Annane D, Bauer M, Bellomo R, Bernard GR, Chiche JD, Coopersmith CM, *et al*: The third international consensus definitions for sepsis and septic shock (sepsis-3). JAMA 315: 801-810, 2016.
50. Giamarellos-Bourboulis EJ, Aschenbrenner AC, Bauer M, Bock C, Calandra T, Gat-Viks I, Kyriazopoulou E, Lupse M, Monneret G, Pickkers P, *et al*: The pathophysiology of sepsis and precision-medicine-based immunotherapy. Nat Immunol 25: 19-28, 2024.
51. Saxena J, Das S, Kumar A, Sharma A, Sharma L, Kaushik S, Kumar Srivastava V, Jamal Siddiqui A and Jyoti A: Biomarkers in sepsis. Clin Chim Acta 562: 119891, 2024.

52. Li Y, Liu C, Fang B, Chen X, Wang K, Xin H, Wang K and Yang SM: Ferroptosis, a therapeutic target for cardiovascular diseases, neurodegenerative diseases and cancer. J Transl Med 22: 1137, 2024.
53. Xl L, Gy Z, R G and N C: Ferroptosis in sepsis: The mechanism, the role and the therapeutic potential. Front Immunol 13: 956361, 2022.
54. Li N, Wang W, Zhou H, Wu Q, Duan M, Liu C, Wu H, Deng W, Shen D and Tang Q: Ferritinophagy-mediated ferroptosis is involved in sepsis-induced cardiac injury. Free Radic Biol Med 160: 303-318, 2020.
55. Liu P, Feng Y, Li H, Chen X, Wang G, Xu S, Li Y and Zhao L: Ferrostatin-1 alleviates lipopolysaccharide-induced acute lung injury via inhibiting ferroptosis. Cell Mol Biol Lett 25: 10, 2020.
56. Zheng Q, Xing J, Li X, Tang X and Zhang D: PRDM16 suppresses ferroptosis to protect against sepsis-associated acute kidney injury by targeting the NRF2/GPX4 axis. Redox Biol 78: 103417, 2024.
57. Wei XB, Jiang WQ, Zeng JH, Huang LQ, Ding HG, Jing YW, Han YL, Li YC and Chen SL: Exosome-Derived lncRNA NEAT1 exacerbates sepsis-associated encephalopathy by promoting ferroptosis through regulating miR-9-5p/TFRC and GOT1 axis. Mol Neurobiol 59: 1954-1969, 2022.
58. Huff LA, Yan S and Clemens MG: Mechanisms of Ataxia Telangiectasia Mutated (ATM) control in the DNA damage response to oxidative stress, epigenetic regulation, and persistent innate immune suppression following sepsis. Antioxidants (Basel) 10: 1146, 2021.
59. Chen PH, Tseng WH and Chi JT: The intersection of DNA damage response and ferroptosis-a rationale for combination therapeutics. Biology (Basel) 9: 187, 2020.
60. Chen PH, Wu J, Ding CC, Lin CC, Pan S, Bossa N, Xu Y, Yang WH, Mathey-Prevot B and Chi JT: Kinome screen of ferroptosis reveals a novel role of ATM in regulating iron metabolism. Cell Death Differ 27: 1008-1022, 2020.
61. Wu H, Liu Q, Shan X, Gao W and Chen Q: ATM orchestrates ferritinophagy and ferroptosis by phosphorylating NCOA4. Autophagy 19: 2062-2077, 2023.
62. Jiang J, Ruan Y, Liu X, Ma J and Chen H: Ferritinophagy is critical for deoxynivalenol-induced liver injury in mice. J Agric Food Chem 72: 6660-6671, 2024.
63. Shackelford RE, Fu Y, Manuszak RP, Brooks TC, Sequeira AP, Wang S, Lowery-Nordberg M and Chen A: Iron chelators reduce chromosomal breaks in ataxia-telangiectasia cells. DNA Repair (Amst) 5: 1327-1336, 2006.
64. Shackelford RE, Manuszak RP, Johnson CD, Hellrung DJ, Link CJ and Wang S: Iron chelators increase the resistance of Ataxia telangeictasia cells to oxidative stress. DNA Repair (Amst) 3: 1263-1272, 2004.
65. McDonald CJ, Ostini L, Wallace DF, John AN, Watters DJ and Subramaniam VN: Iron loading and oxidative stress in the Atm-/- mouse liver. Am J Physiol Gastrointest Liver Physiol 300: G554-560, 2011.
66. Wang H, Huang J, Yi W, Li J, He N, Kang L, He Z and Chen C: Identification of immune-related key genes as potential diagnostic biomarkers of sepsis in children. J Inflamm Res 15: 2441-2459, 2022.
67. da Silva Neto Trajano LA, da Silva Sergio LP, de Oliveira DSL, Trajano ETL, Dos Santos Silva MA, de Paoli F, Mencalha AL and da Fonseca AS: Low-power infrared laser modulates mRNA levels from genes of base excision repair and genomic stabilization in heart tissue from an experimental model of acute lung injury. Photochem Photobiol Sci 21: 1299-1308, 2022.
68. Gao T, Gao S, Wang H, Wang S, Li L, Hu J, Yan S, Zhang R, Zhou Y and Dong H: Garlic ameliorates atherosclerosis by regulating ferroptosis pathway: An integrated strategy of network pharmacology, bioinformatic and experimental verification. Front Pharmacol 15: 1388540, 2024.
69. Zhu F, Zou D, Shi P, Tang L, Wu D, Hu X, Yin F and Liu J: Dipeptidyl peptidase 4: A predictor of ferroptosis in ulcerative colitis. J Gene Med 26: e3742, 2024.
70. Liu R, Li F, Hao S, Hou D, Zeng X, Huang H, Sethi G, Guo J and Duan C: Low-dose olaparib improves septic cardiac function by reducing ferroptosis via accelerated mitophagy flux. Pharmacol Res 200: 107056, 2024.
71. Ng PY, Ng AK, Ip A, Wu MZ, Guo R and Yiu KH: Risk of ICU admission and related mortality in patients with sodium-glucose cotransporter 2 inhibitors and dipeptidyl peptidase-4 inhibitors: A territory-wide retrospective cohort study. Crit Care Med 51: 1074-1085, 2023.
72. Wu MZ, Chandramouli C, Wong PF, Chan YH, Li HL, Yu SY, Tse YK, Ren QW, Yu SY, Tse HF, *et al*: Risk of sepsis and pneumonia in patients initiated on SGLT2 inhibitors and DPP-4 inhibitors. Diabetes Metab 48: 101367, 2022.
73. Zhou Y, Chen Y, Li J, Fu Z, Chen Q, Zhang W, Luo H and Xie M: The development of endoplasmic reticulum-related gene signatures and the immune infiltration analysis of sepsis. Front Immunol 14: 1183769, 2023.
74. Xu J, Zhu M, Luo P and Gong Y: Machine learning screening and validation of panoptosis-related gene signatures in sepsis. J Inflamm Res 17: 4765-4780, 2024.
75. Wu XL and Guo YN: Role of cellular senescence genes and immune infiltration in sepsis and sepsis-induced ARDS based on bioinformatics analysis. J Inflamm Res 17: 9119-9133, 2024.
76. Luo S, Lyu Z, Ge L, Li Y, Liu Y, Yuan Y, Zhao R, Huang L, Zhao J, Huang H and Luo Y: Ataxia telangiectasia mutated protects against lipopolysaccaride-induced blood-brain barrier disruption by regulating ATK/DRP1-mediated mitochondrial homeostasis. Shock 60: 100-109, 2023.
77. Figueiredo N, Chora A, Raquel H, Pejanovic N, Pereira P, Hartleben B, Neves-Costa A, Moita C, Pedroso D, Pinto A, *et al*: Anthracyclines induce DNA damage response-mediated protection against severe sepsis. Immunity 39: 874-884, 2013.
78. Vliegen G, Kehoe K, Bracke A, De Hert E, Verkerk R, Fransen E, Jongers B', Peters E, Lambeir AM, Kumar-Singh S, *et al*: Dysregulated activities of proline-specific enzymes in septic shock patients (sepsis-2). PLoS One 15: e0231555, 2020.
79. Chen G, Zhang W, Wang C, Hu Y and Li S: Screening therapeutic core genes in sepsis using network pharmacology and single-cell RNA sequencing. Biochem Genet: March 20, 2025 (Epub ahead of print).
80. Rim J, Gallini J, Jasien C, Cui X, Phillips L, Trammell A and Sadikot RT: Use of oral anti-diabetic drugs and risk of hospital and intensive care unit admissions for infections. Am J Med Sci 364: 53-58, 2022.
81. Brabenec L, Müller M, Hellenthal KEM, Karsten OS, Pryvalov H, Otto M, Holthenrich A, Matos ALL, Weiss R, Kintrup S, *et al*: Targeting procalcitonin protects vascular barrier integrity. Am J Respir Crit Care Med 206: 488-500, 2022.
82. Wang SC, Wang XY, Liu CT, Chou RH, Chen ZB, Huang PH and Lin SJ: The dipeptidyl peptidase-4 inhibitor linagliptin ameliorates endothelial inflammation and microvascular thrombosis in a sepsis mouse model. Int J Mol Sci 23: 3065, 2022.
83. Kröller-Schön S, Knorr M, Hausding M, Oelze M, Schuff A, Schell R, Sudowe S, Scholz A, Daub S, Karbach S, *et al*: Glucose-independent improvement of vascular dysfunction in experimental sepsis by dipeptidyl-peptidase 4 inhibition. Cardiovasc Res 96: 140-149, 2012.
84. Steven S, Hausding M, Kröller-Schön S, Mader M, Mikhed Y, Stamm P, Zinßius E, Pfeffer A, Welschof P, Agdauletova S, *et al*: Gliptin and GLP-1 analog treatment improves survival and vascular inflammation/dysfunction in animals with lipopolysaccharide-induced endotoxemia. Basic Res Cardiol 110: 6, 2015.
85. Zhang N, Tang S, Zhang J, Pei B, Pang T and Sun G: The dipeptidyl peptidase-4 inhibitor linagliptin ameliorates LPS-induced acute lung injury by maintenance of pulmonary microvascular barrier via activating the Epac1/AKT pathway. Biomed Pharmacother 155: 113704, 2022.
86. Delic D, Klein T, Wohnhaas CT, Feng H, Lin X, Zhang JR and Wu D: Dipeptidyl peptidase-4 inhibitor linagliptin reduces inflammatory response, ameliorates tissue edema formation, and improves survival in severe sepsis. Biomed Pharmacother 182: 117778, 2025.
87. Steven S, Jurk K, Kopp M, Kröller-Schön S, Mikhed Y, Schwierczek K, Roohani S, Kashani F, Oelze M, Klein T, *et al*: Glucagon-like peptide-1 receptor signalling reduces microvascular thrombosis, nitro-oxidative stress and platelet activation in endotoxaemic mice. Br J Pharmacol 174: 1620-1632, 2017.
88. Dai W, Zheng P, Luo D, Xie Q, Liu F, Shao Q, Zhao N and Qian K: LPIN1 is a regulatory factor associated with immune response and inflammation in sepsis. Front Immunol 13: 820164, 2022.
89. He S, He Y, Deng L, Guo Y, Wang X, Wang Q, Luo L and Liu Q: Identification of RRM2 as a key ferroptosis-related gene in sepsis. Inflamm Res 73: 459-473, 2024.
90. Liu CY, Yang YS, Pei MQ, Zhang Y, Chen WC, Liang JW and He HF: Systematic analysis based on bioinformatics and experimental validation identifies Alox5 as a novel therapeutic target of quercetin for sepsis. Ann Med 56: 2411015, 2024.
91. Pei S, Liu J, Wang Z, Fan Y, Meng S, Huang X, Cui Y and Xie K: Genetic analysis of diagnostic and therapeutic potential for ferroptosis in postoperative sepsis. Int Immunopharmacol 147: 114042, 2025.

92. Martin MD, Badovinac VP and Griffith TS: CD4 T Cell Responses and the Sepsis-Induced Immunoparalysis State. Front Immunol 11: 1364, 2020.
93. Heidarian M, Griffith TS and Badovinac VP: Sepsis-induced changes in differentiation, maintenance, and function of memory CD8 T Cell subsets. Front Immunol 14: 1130009, 2023.
94. Kong Z, Cai S, Xie W, Chen J, Xie J, Yang F, Li Z, Bai X and Liu T: CD4 + T Cells ferroptosis is associated with the development of sepsis in severe polytrauma patients. Int Immunopharmacol 127: 111377, 2024.
95. Qu G, Liu H, Li J, Huang S, Zhao N, Zeng L and Deng J: GPX4 is a key ferroptosis biomarker and correlated with immune cell populations and immune checkpoints in childhood sepsis. Sci Rep 13: 11358, 2023.
96. Wu J, Liu Q, Zhang X, Tan M, Li X, Liu P, Wu L, Jiao F, Lin Z and Wu X: The interaction between STING and NCOA4 exacerbates lethal sepsis by orchestrating ferroptosis and inflammatory responses in macrophages. Cell Death Dis 13: 653, 2022.